

# Stress relaxation and thermo-visco-elastic effects in fluid-filled slits and fluid-loaded plates

Erik García Neefjes<sup>1</sup>, David Nigro<sup>2</sup>, Raphaël C. Assier<sup>3</sup>,  
William J. Parnell<sup>3</sup>

<sup>1</sup> School of Mathematical and Physical Sciences, Macquarie University, Sydney NSW 2109, Australia

<sup>2</sup>Thales United Kingdom, 350 Longwater Avenue Green Park, Reading RG2 6GF, UK

<sup>3</sup>Department of Mathematics, University of Manchester, Oxford Rd, Manchester, M13 9PL, UK

March 19, 2024

## Abstract

In this paper, we theoretically analyse wave propagation in two canonical problems of interest: fluid-filled thermo-visco-elastic slits and fluid-loaded thermo-visco-elastic plates. We show that these two configurations can be studied via the same pair of dispersion equations with the aid of the framework developed in [1], which incorporates thermal effects. These two problems are further interrelated, since in the short wavelength limit (relative to the slit/plate width) the respective modes are governed by the same dispersion equation, commonly known as the Scholte–Stoneley equation. It is the Scholte-type modes that are mainly analyzed in this paper. We illustrate results when the fluid is water, although the theory is valid for any Newtonian fluid. Both ‘hard’ and ‘soft’ solids are compared, with the emphasis being placed on the importance of thermo-viscoelastic effects, particularly when *stress relaxation* is considered. Two main recent works are discussed extensively, namely [2] for slits and [3] for loaded plates, both of which do not incorporate viscoelastic mechanisms. We show how the consideration of viscoelasticity can extend the results discussed therein, and explain the circumstances under which they arise.

## 1 Introduction

Acoustic and elastic wave propagation in confined ducts, channels/slits and in plates is a classical field with a broad range of applications [4, 5]. Loss mechanisms in a variety of such geometries are still of significant interest from a research perspective, particularly when these configurations are employed as the microstructures in metamaterials. As an example, partly motivated by experimental work in [6] for air-filled channels, the work in [2] considered acoustic propagation in water-filled steel slits. Specifically the study focused on the importance of boundary layer attenuation in the fluid region as the slits become narrow. It was found that although the presence of fluid viscosity is necessary to describe the attenuation of the mode along the slit, in order to capture the large reduction in phase speed as the width decreases, it is key to capture the fluid-structure interaction (FSI) effects, as is well known in underwater acoustics. On the other hand, for air-filled slits, FSI may be ignored in most instances, even for considerably soft media such as rubbers [1], but instead, thermal dissipative effects should be taken into account [7, 8] as opposed to water under normal circumstances [9].

One of the main objectives of this paper is to extend the analysis in [2] to the case of *soft* solid slits/plates and in particular to take into account viscoelastic losses in such soft solids. Following

the discussion above, in order to exploit these mechanisms for fluid-filled slits, it is required to have strong FSI effects and therefore only results for water are considered, although the theory is applicable to any Newtonian fluid. The fluid-solid half-space which has been widely studied under many circumstances [10, 11, 12, 13], is considered first since it constitutes the geometrical limit as the channel width increases (relative to the wavelength of the transverse wave in the fluid). This configuration gives rise to two well known main families of interface wave solutions corresponding to *Leaky-Rayleigh* (LR) and *Stoneley-Scholte* (Sc) modes. Unlike the LR [14], the Sc mode propagates for any fluid-solid interface and in particular is the only propagating mode for water-soft interfaces [13], which we consider here. The Sc phase speed is reduced significantly for ‘soft’ fluid-solid interfaces [3] as opposed to ‘hard’ fluid-solid interfaces where the Sc phase speed is approximately equal to the speed of sound in the fluid. The influence of viscoelasticity on this mode for water-soft media (synthetic resins) is studied theoretically and experimentally in a series of papers [12, 15, 16] with the objective of using Sc waves to characterise the properties of the ocean’s sedimentary bottom.

In the current work, we bring special attention to the importance of viscoelastic *stress relaxation* in the phase-speed and attenuation of the Sc mode (and body waves) and the corresponding regimes where these effects become important. Under the standard linear solid model (SLSM) used here, the key dimensionless parameter in the frequency domain is the *Deborah number*  $\omega t_r$ , where  $\omega$  is the angular frequency and  $t_r$  the single relaxation time of the material under consideration [1]. Although the relaxation times of soft materials can vary over several orders of magnitude [17], the frequencies involved in the majority of reported studies are such that  $\omega t_r \gg 1$ , which we presume is the reason for the lack of stress relaxation analyses in the form presented in this paper. Despite this, we believe the regime considered here remains of strong interest since these effects are clearly visible in experiments [18], and the importance of stress relaxation is often reported in the literature [3, 19].

Another important part of this paper is devoted to the study of (thermo-viscous) fluid-loaded plates. In spite of the fact that this configuration is physically different to the case of fluid-filled slits, the associated dispersion equations (DEs) are in fact identical in both problems thanks to the generality of the media considered [1]. Early work on fluid-loaded plates [20, 21] identified that the presence of the liquid causes the standard plate Lamb wave solutions to become *leaky* (as for Rayleigh modes in the half-space) and another two solutions arise which are not present in the absence of the fluid. These solutions are in fact Scholte-like interface waves which become coupled in the plate region as the thicknesses decreases, and in order to distinguish them from their half-space counterpart we define them as ‘coupled plate-Scholte’ modes [3]. Many works have been focused around the consequences of attenuation due to fluid viscosity [22, 23, 24, 25] on the modes of fluid-loaded plates. Nevertheless, the majority of these studies have been based around ‘hard’ interfaces, presumably since this is the regime most common in sensing and non-destructive applications. Recently in [3] the case of water-loaded acrylic plates, which is a ‘soft’ interface, was considered, and it was illustrated that significant differences arise in the phase speed of the coupled plate-Sc with respect to standard metal interfaces. In particular, they justified and experimentally demonstrated the dispersive behaviour of the symmetric coupled plate-Scholte mode which had previously only been characterized for soft films at very high frequencies [26]. Although not provided in their analysis, it is remarked in the experimental verification of [3] the importance of viscoelastic properties of soft media, and in particular the importance of stress relaxation under particular frequency ranges. In this paper, we contribute to the theory in this study, by taking into account these dissipative mechanisms in order to assess their influence (and that of boundary layers) in both the symmetric and anti-symmetric coupled plate-Scholte modes for a wide range of plate thicknesses, and frequencies.

In Section 2, we briefly introduce the visco-elastic (VE) formulation that we will employ throughout this work which allows us to simultaneously consider (visco)elastic solid and visco-acoustic fluid media as explained in [1]. We discuss two classical models to capture the frequency dependence of the elastic moduli, namely the Kelvin–Voigt model (KVM) and the SLSM. These two models will be compared repeatedly in this work. In Section 3 we analyse the single interface configuration consisting of two half-space media in perfect contact. By seeking interface solutions to this set-up, we derive the *Stoneley* DE, from which the *Scholte* and *Rayleigh* DEs can be obtained by considering the inviscid fluid and zero density limits respectively. The Stoneley and Scholte DEs give rise to Sc and LR waves which we discuss in detail. Since our fluid of interest is water, we study ‘hard’ and ‘soft’ interfaces (definitions are provided) by considering material parameters associated to steel and PVC, and investigate thermo-viscous effects. For the soft case, we analyse the additional behaviour that arises when the SLSM is employed.

In Section 4 we consider the double interface configuration, with the finite width medium constituting the slit/plate. We show how generalised DEs for symmetric/anti-symmetric modes valid for both configurations can be obtained. These equations recover more common forms found in the literature when certain effects are neglected such as the fluid’s viscosity, which is illustrated. In the short wavelength-limit the general DEs reduce to the half-space Stoneley DE considered in Section 3, which is used as the initial value of the recursive root finding technique. For the slits, we show how the softness of the solid, together with viscoelastic damping gives rise to rather different results to those presented for water-filled steel slits in [2], and we confirm the claim made therein, namely that including thermal effects do not introduce any notable effects (within the considered regions of parameter space).

For plates, both the symmetric/anti-symmetric coupled plate-Scholte modes are considered, and we observe the dispersive behaviour for the symmetric mode for soft plates reported recently in [3]. We extend the theoretical analysis in [3] by including the effect of thermo-viscous boundary layer attenuation (which is minimal) as well as viscoelastic damping in the solid which we show can be very important, especially near the *glass transition* of the moduli. The presence of a global maximum of the attenuation as a function of plate thickness for the symmetric mode is highlighted. We finish with conclusions in Section 5. The general framework with the inclusion of thermal effects is devoted to Appendix A, together with the equivalent TVE dispersion equations and a final note on the comparisons of TVE and VE solutions.

## 2 Governing equations for linear, isotropic VE continua

We assume that the media under consideration here are linear, isotropic and further we make the approximation that all deformations are *isothermal*, so that thermo-mechanical coupling need not be taken into account (these effects are instead discussed in Appendix A). Consequently, the energy balance equation is automatically satisfied, so that the focus is to solve the linearised equation of motion, namely

$$\nabla \cdot \hat{\boldsymbol{\sigma}} = \rho_0 \frac{\partial^2 \hat{\mathbf{u}}}{\partial t^2}, \quad (2.1)$$

where  $\rho_0$  denotes the constant mass density,  $\hat{\mathbf{u}} = \{\hat{u}_x, \hat{u}_y, \hat{u}_z\}$  the continuum’s displacement vector,  $\nabla$  is the vectorial gradient operator and  $\hat{\boldsymbol{\sigma}}$  is the Cauchy stress tensor which must capture all the required properties of the media we want to consider. Hereditary integrals give a general way to

express the VE constitutive behaviour of the medium (e.g. [27], Chapter 1)

$$\hat{\boldsymbol{\sigma}} = \int_{-\infty}^t 2\hat{\mu}(t-\mathcal{T}) \frac{\partial \hat{\boldsymbol{\varepsilon}}(\mathcal{T})}{\partial \mathcal{T}} d\mathcal{T} + \left( \int_{-\infty}^t \hat{K}(t-\mathcal{T}) \operatorname{tr} \left( \frac{\partial \hat{\boldsymbol{\varepsilon}}(\mathcal{T})}{\partial \mathcal{T}} \right) d\mathcal{T} \right) \mathbf{I}, \quad (2.2)$$

where  $\hat{\boldsymbol{\varepsilon}} = (\nabla \hat{\mathbf{u}} + (\nabla \hat{\mathbf{u}})^T)/2$  is the linearised strain tensor,  $\operatorname{tr}(\cdot)$  the trace operator,  $\mathbf{I}$  the identity tensor and  $\hat{\boldsymbol{\varepsilon}} = \hat{\boldsymbol{\varepsilon}} - \operatorname{tr}(\hat{\boldsymbol{\varepsilon}})\mathbf{I}/3$  represents the off-diagonal terms of the strain tensor. Further,  $\hat{\mu}(t)$ ,  $\hat{K}(t)$  are time-dependent (visco) elastic moduli, which must be identically zero for  $t < 0$  to obey causality and are such that the integrals in (2.2) are convergent. In this paper we will be considering time-harmonic disturbances, so that all the fields satisfy

$$\{\hat{\mathbf{u}}, \hat{\boldsymbol{\sigma}}, \hat{\boldsymbol{\varepsilon}}, \hat{\boldsymbol{\varepsilon}}\}(\mathbf{x}, t) = \operatorname{Re} \{ \{ \mathbf{u}, \boldsymbol{\sigma}, \boldsymbol{\varepsilon}, \boldsymbol{\varepsilon} \}(\mathbf{x}) e^{-i\omega t} \}, \quad (2.3)$$

which when substituted in (2.2), (2.1) and factoring out the common term give respectively

$$\boldsymbol{\sigma} = 2\mu(\omega)\boldsymbol{\varepsilon} + K(\omega) \operatorname{tr}(\boldsymbol{\varepsilon})\mathbf{I}, \quad (2.4a)$$

$$(K(\omega) + \frac{4}{3}\mu(\omega))\nabla(\nabla \cdot \mathbf{u}) - \mu(\omega)\nabla \times \nabla \times \mathbf{u} + \rho_0\omega^2\mathbf{u} = \mathbf{0}, \quad (2.4b)$$

where  $\mu(\omega)$ ,  $K(\omega)$  are scaled Fourier transforms of the original moduli [1]. On adopting the Helmholtz decomposition

$$\mathbf{u} = \nabla\phi + \nabla \times \boldsymbol{\Phi}, \quad (2.5)$$

with  $\nabla \cdot \boldsymbol{\Phi} = 0$ , the compressional and shear wave potentials  $\phi$ ,  $\boldsymbol{\Phi}$  must respectively satisfy

$$(\Delta + k_\phi^2)\phi = 0, \quad k_\phi^2(\omega) = \frac{\rho_0\omega^2}{K(\omega) + \frac{4}{3}\mu(\omega)}, \quad (2.6a)$$

$$(\Delta + k_\Phi^2)\boldsymbol{\Phi} = \mathbf{0}, \quad k_\Phi^2(\omega) = \frac{\rho_0\omega^2}{\mu(\omega)}, \quad (2.6b)$$

recalling that the material parameters appearing in the compressional/shear wavenumbers  $k_\phi$ ,  $k_\Phi$  in (2.6) are isothermal, which is particularly important to consider for viscous gases such as air (since the isothermal bulk modulus can differ significantly from the corresponding more common adiabatic modulus) [1]. Given the shear and bulk moduli present in (2.6), we can define the generalized first Lamé coefficient, Poisson's ratio and Young's modulus respectively as [28]

$$\lambda(\omega) = K(\omega) - \frac{2}{3}\mu(\omega), \quad \nu(\omega) = \frac{3K(\omega) - 2\mu(\omega)}{6K(\omega) + 2\mu(\omega)}, \quad E(\omega) = \frac{9K(\omega)\mu(\omega)}{3K(\omega) + \mu(\omega)}. \quad (2.7)$$

There exist plenty of models to capture the frequency dependence of these moduli which are appropriate in particular circumstances (e.g. [29]), but in this work we focus on the Kelvin–Voigt Model (KVM) (which we also refer to as local VE) and the Standard Linear Solid Model (SLSM), which are discussed extensively in [1] starting from their time domain behaviour. For a given modulus  $\mathcal{M}(\omega)$  we have

$$\text{(KVM)} \quad \mathcal{M}(\omega) = \mathcal{M}_0 - i\omega\eta_{\mathcal{M}}, \quad (2.8a)$$

$$\text{(SLSM)} \quad \mathcal{M}(\omega) = \mathcal{M}_\infty - (\mathcal{M}_0 - \mathcal{M}_\infty) \frac{i\omega t_r}{1 - i\omega t_r} = \frac{\mathcal{M}_\infty + \mathcal{M}_0(\omega t_r)^2}{1 + (\omega t_r)^2} - i \frac{(\mathcal{M}_0 - \mathcal{M}_\infty)\omega t_r}{1 + (\omega t_r)^2}. \quad (2.8b)$$

In the KVM, the real part ( $\mathcal{M}_0$ ) is fixed and the (attenuative) imaginary part known as the *loss modulus* is characterized by  $\omega\eta_{\mathcal{M}}$  where  $\eta_{\mathcal{M}}$  is a constant viscosity coefficient. In the SLSM,  $\mathcal{M}_\infty$ ,  $\mathcal{M}_0$

correspond to the long-term and instantaneous moduli and  $t_r$  represents the (single) relaxation time of the material. The Deborah number  $\omega t_r$  in (2.8b), relates the characteristic time of the problem ( $1/\omega$ ) with the relaxation time of the material in consideration. The moduli further satisfy  $\mathcal{M}_\infty \leq \mathcal{M}_0$ , with the equality implying the medium is perfectly elastic. We note that for  $\omega t_r \gg 1$ ,  $\mathcal{M} \rightarrow \mathcal{M}_0$  and conversely for  $\omega t_r \ll 1$ ,  $\mathcal{M} \rightarrow \mathcal{M}_\infty$  and therefore higher frequencies correspond to the *glassy* (stiffer) phase of the materials and lower frequencies to a *rubbery* (softer) phase. The loss modulus has a global maximum at  $\omega t_r = 1$  which defines the *glass transition region*, and therefore it is in the vicinity of this region where the majority of intrinsic VE losses are manifested.

Visco-acoustic (Newtonian) fluids can also be described by (2.4)-(2.6) with  $\mu(\omega) = -i\omega\eta_\mu$ , where  $\eta_\mu > 0$  is the kinematic viscosity [1, 23, 25], so that the square of the shear wavenumber becomes purely imaginary, i.e.  $k_\Phi^2 = i/\delta_\nu^2$  where  $\delta_\nu = \sqrt{\eta_\mu/\rho_0\omega}$  is a boundary layer parameter related to the common Stokes' boundary layer thickness by  $\delta_s = 2\pi\sqrt{2}\delta_\nu$ .

### 3 Single interface: Two VE half-spaces in perfect contact

We first seek interface waves associated with the configuration of VE-VE half-spaces separated by an interface at  $y = 0$ , as seen on the left of Figure 1. From the resulting DEs we can determine the Leaky Rayleigh and Scholte–Stoneley modes and analyse some of their key properties. As we will observe in the next section, the understanding of the half-space will facilitate the study of the double interface configuration (right of Figure 1).

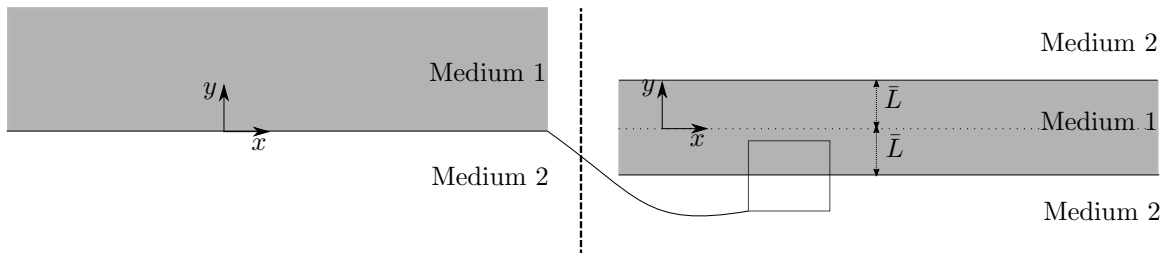


Figure 1: Schematic representations of the 2D geometric configurations considered in this paper, noting that all media are infinitely extending in the  $x$ -direction. Left: Two semi-infinite VE continua as considered in Section 3 (single interface). Right: A VE medium of width  $\bar{W} = 2\bar{L}$  bounded by two semi-infinite VE media as considered in Section 4 (double interface).

#### 3.1 The Stoneley, Rayleigh and Scholte Dispersion Equations

In Section 2 all the relevant equations were given in dimensional form. It will be convenient in the subsequent analysis to have a notational distinction between dimensional/non-dimensional quantities and therefore from here onwards we will introduce an over-bar  $\bar{\cdot}$  to all dimensional quantities. We seek potential solutions to the governing equations (2.4) that decay away from the boundary in each half-space, since interface waves can be represented as a linear combination of these four waves:

$$\bar{\phi}_1 = \bar{P}_1 e^{-\bar{\gamma}_{\phi_1} \bar{y} + i \bar{k} \bar{x}}, \quad \bar{\phi}_2 = \bar{P}_2 e^{\bar{\gamma}_{\phi_2} \bar{y} + i \bar{k} \bar{x}}, \quad (3.1a)$$

$$\bar{\Phi}_1 = \bar{S}_1 e^{-\bar{\gamma}_{\Phi_1} \bar{y} + i \bar{k} \bar{x}}, \quad \bar{\Phi}_2 = \bar{S}_2 e^{\bar{\gamma}_{\Phi_2} \bar{y} + i \bar{k} \bar{x}}, \quad (3.1b)$$

where

$$\bar{\gamma}_{\phi_1} = (\bar{k}^2 - \bar{k}_{\phi_1}^2)^{1/2}, \quad \bar{\gamma}_{\phi_2} = (\bar{k}^2 - \bar{k}_{\phi_2}^2)^{1/2}, \quad \bar{\gamma}_{\Phi_1} = (\bar{k}^2 - \bar{k}_{\Phi_1}^2)^{1/2}, \quad \bar{\gamma}_{\Phi_2} = (\bar{k}^2 - \bar{k}_{\Phi_2}^2)^{1/2}, \quad (3.2)$$

for some complex amplitudes  $\bar{P}_1, \bar{P}_2, \bar{S}_1, \bar{S}_2$ . We must ensure that the choice of the various branch cuts of the square root functions in (3.2) is consistent with causality, which is further discussed below. At the interface between the two media, the solutions must satisfy continuity of traction and displacement boundary conditions (BCs), that is on  $\bar{y} = 0$ ,

$$\bar{\sigma}_{yy}^1 = \bar{\sigma}_{yy}^2, \quad \bar{\sigma}_{xy}^1 = \bar{\sigma}_{xy}^2, \quad \bar{\mathbf{u}}_1 = \bar{\mathbf{u}}_2. \quad (3.3)$$

Substitution of (3.1) into (3.3) then leads to the VE Stoneley DE, that is

$$\begin{aligned} \bar{D}_{St} = \bar{c}^4 [(\bar{\rho}_1 - \bar{\rho}_2)^2 - (\bar{\rho}_2 A_1 + \bar{\rho}_1 A_2)(\bar{\rho}_2 B_1 + \bar{\rho}_1 B_2)] \\ + 2\bar{c}^2 \bar{Q}(-\bar{\rho}_2 A_1 B_1 + \bar{\rho}_1 A_2 B_2 - \bar{\rho}_1 + \bar{\rho}_2) + \bar{Q}^2 (A_1 B_1 - 1)(A_2 B_2 - 1) = 0, \end{aligned} \quad (3.4)$$

which for a purely elastic–elastic interface takes the form as in Stoneley’s original paper [30], (as expected prior to the specification of the frequency dependence of the elastic moduli due to the correspondence principle for elasticity see e.g. [29]) with

$$\bar{c} = \frac{\bar{\omega}}{\bar{k}}, \quad \{A_1, A_2, B_1, B_2\} = \frac{1}{\bar{k}} \{\bar{\gamma}_{\phi_1}, \bar{\gamma}_{\phi_2}, \bar{\gamma}_{\Phi_1}, \bar{\gamma}_{\Phi_2}\}, \quad \bar{Q} = 2(\bar{\rho}_1 \bar{c}_{\Phi_1}^2 - \bar{\rho}_2 \bar{c}_{\Phi_2}^2), \quad (3.5)$$

where  $\bar{c}_{\Phi} = \bar{\omega}/\bar{k}_{\Phi}$  in each medium. When thermal effects are considered, (3.4) takes the more complex form (A.11), as discussed in Appendix A.2. If we let the density of the upper medium vanish, i.e.  $\bar{\rho}_1 \rightarrow 0$  in (3.4), after some manipulation using (3.5) we obtain the Rayleigh DE, namely

$$\bar{D}_{Ra} = (2\bar{k}^2 - \bar{k}_{\Phi_2}^2)^2 - 4\bar{k}^2 \bar{\gamma}_{\phi_2} \bar{\gamma}_{\Phi_2} = 0, \quad (3.6)$$

which governs the ubiquitous *Rayleigh waves*, originally described in [31] for elastic media. Alternatively, in the inviscid fluid limit  $\bar{\mu}_1(\omega) \rightarrow 0$ , it follows that  $\bar{k}_{\Phi_1}^2 \rightarrow \infty$  and hence  $\bar{\gamma}_{\Phi_1}, B_1 \rightarrow \infty$  whereas  $\bar{Q} \rightarrow -2\bar{\rho}_2 \bar{c}_{\Phi_2}^2$  so that (3.4) becomes

$$\bar{D}_{Sc} = \bar{D}_{Ra} + \frac{\bar{\gamma}_{\phi_2} \bar{k}_{\Phi_2}^4}{\bar{\gamma}_{\phi_1} \rho_s} = 0, \quad \text{with} \quad \rho_s = \frac{\bar{\rho}_2}{\bar{\rho}_1}, \quad (3.7)$$

which is the common Scholte DE (also referred to as Scholte–Stoneley DE [3]). As we will discuss shortly, in general (3.7) and (3.4) admit two families of interface wave solutions, namely *Leaky Rayleigh* and *Scholte* waves. Direct observation of (3.7) illustrates the role of the density ratio  $\rho_s$ , when  $\rho_s \gg 1$  i.e. for “hard” interfaces, the fluid-loading term will have negligible influence and therefore the behaviour of  $\bar{D}_{Sc}$  can be seen as a small perturbation to  $\bar{D}_{Ra}$ . Nevertheless, for softer interfaces such that  $\rho_s \approx 1$  significantly different behaviour of the spectrum can be expected.

Naturally, due to the symmetry of the configuration, (3.6) and (3.7) can also be recovered by taking the limits  $\bar{\rho}_2 \rightarrow 0, \bar{\mu}_2(\omega) \rightarrow 0$  respectively (and interchanging the subscripts ‘1’ and ‘2’ in the subsequent equations). Despite the interest of this work being on losses in fluid–solid configurations, this symmetry property makes the use of the general VE–VE configuration convenient, which will become apparent in Section 4 where we will be able to consider two physically different problems with the same set of DEs.

The roots of (3.4), (3.6), (3.7), (A.11) and the various DEs studied in Section 4 are calculated using the MATLAB [version 9.8.0.1380330 (R2020a)] command *fsolve*, which finds the local zero of a

function close to a given starting point specified by the user. This initial value will differ depending on the mode under consideration, as we will specify below.

Throughout the paper, the several square root functions (3.2) are chosen such that, as  $|\bar{k}| \rightarrow \infty$   $\bar{\gamma}_{\phi_1}, \bar{\gamma}_{\phi_2}, \bar{\gamma}_{\Phi_1}, \bar{\gamma}_{\Phi_2} \rightarrow \bar{k}$ , with the branch cuts from  $\bar{k}_{\phi_1}, \bar{k}_{\phi_2}, \bar{k}_{\Phi_1}, \bar{k}_{\Phi_2}$  taken in the upper half-plane and those from  $-\bar{k}_{\phi_1}, -\bar{k}_{\phi_2}, -\bar{k}_{\Phi_1}, -\bar{k}_{\Phi_2}$  taken in the lower half-plane. The branch cuts are chosen to run with fixed real parts (i.e. parallel to the imaginary axis) from the respective branch points. We note that in order to analyse *all* roots of these equations, in principle it is necessary to consider all possible combinations of Riemann sheets giving e.g.  $2^4$  for (3.4),  $2^3$  for (3.7),  $2^2$  for (3.6) and  $2^6$  for (A.11), see e.g. [14, 32, 33]. In this work, we are concerned with the influence of TVE effects on the well established roots of these equations, so we simply need to make sure the obtained solutions are causal and do not jump Riemann sheets. On top of this, we ensure they behave as expected in the absence of any form dissipation.

In what follows, the roots of the DEs will be plotted in terms of non-dimensional phase speed and attenuation, which are given by

$$\text{Phase Speed} = \frac{\bar{v}}{\bar{c}_{\square}} = \frac{\text{Re}\{\bar{c}\}}{\bar{c}_{\square}} = \frac{\bar{\omega}}{\text{Re}\{\bar{k}\}\bar{c}_{\square}}, \quad (3.8a)$$

$$\text{Attenuation (dB/wavelength)} = 40\pi \frac{\text{Im}\{\bar{k}\}}{\text{Re}\{\bar{k}\}} \log_{10}(e), \quad (3.8b)$$

where  $\bar{c}_{\square}$  represents a particular sound velocity which we assume constant. In particular  $\bar{c}_0$  denotes the speed of sound of water, and  $\bar{c}_s$  is the lossless shear wave speed of sound in a certain solid material (from Table 1 water gives  $\bar{c}_0 = 1490$  m/s, steel  $\bar{c}_s = 3000$  m/s, and PVC  $\bar{c}_s = 1100$  m/s).

### 3.2 Material parameters: hard/soft solids

We have seen above that different limits of the density ratio  $\rho_s$  can give some insights on the importance of certain terms in the various DEs above. Generally, knowing whether a given fluid–solid pair is hard/soft is intuitive although in some instances this can lead to ambiguity, as recently noticed in [3], which is focused on the Scholte mode solution to (3.7). Indeed, a common definition is whether the material parameters are such that  $\text{Re}\{\bar{k}_{\phi}\} < \text{Re}\{\bar{k}_{\Phi}\} \leq \text{Re}\{\bar{k}_F\}$  or  $\text{Re}\{\bar{k}_{\phi}\} \leq \text{Re}\{\bar{k}_F\} < \text{Re}\{\bar{k}_{\Phi}\}$  which correspond to hard or soft respectively, as in e.g. [13]. Note that since we are fixing materials 1/2 to be fluid/solid respectively (for definition purposes) we have written  $\bar{k}_F \equiv \bar{k}_{\phi_1}$  for the visco-acoustic wavenumber, and  $\bar{k}_{\phi} \equiv \bar{k}_{\phi_2}$ ,  $\bar{k}_{\Phi} \equiv \bar{k}_{\Phi_2}$  corresponding to the standard pressure and shear VE wavenumbers. Nevertheless, in some instances the definition implied by the inequalities can be physically inaccurate e.g. it is shown in [3] by considering the transition between  $\text{Re}\{\bar{k}_{\Phi}\}$ , and  $\text{Re}\{\bar{k}_F\}$  that the Scholte mode’s phase speed remains constant (which should not be the case when transitioning between a ‘hard’ and ‘soft’ solid). For this reason, in that work a hard interface is defined as one where the Scholte velocity is approximately equal to the speed of sound in the fluid, and conversely a soft interface is one where the Scholte velocity is notably less than the speed of sound in the fluid. As a result, the latter definition is more inspired by the actual physics, whereas the former indicated by the inequalities above is purely motivated by the complex plane spectrum. In [11] the same idea is discussed in terms of acoustic impedance of the fluid/solid pair.

VE Parameter Values (Kelvin–Voigt Model)						
Parameter	Unit	Symbol	Water	Steel	PVC	$M_{\tau=0.9}$
Background density	kg/m <sup>3</sup>	$\rho_0$	1000	7871	1360	2011
Shear modulus	GPa	$\mu_0$	–	70.839	1.65	8.55
Bulk modulus (Adiabatic)	GPa	$K_0$	2.2222	189.54	5.0415	24.342
Young’s modulus (Adiabatic)	GPa	$E_0$	–	–	4.4524	–
Dynamic shear viscosity	Pa·s	$\eta_\mu$	$10^{-3}$	$1.85 \times 10^{-5}$	0.1	0.09
Dynamic bulk viscosity	Pa·s	$\eta_K$	$3 \times 10^{-3}$	$1.1 \times 10^{-5}$	0.3	0.27

Table 1: Parameter values for water, steel and PVC used in calculations, taken from [34], [2] and [12] respectively, assumed to be independent of frequency.  $M_{\tau=0.9}$  is defined in (3.9). The PVC values are only applicable for local VE (KVM); the values for the stress relaxation discussion are given in Sections 3.3.3, 4.3.3 and 4.4.3. The additional thermal parameters required for the TVE calculations are provided in Table 2.

Our primary physical interest here is in water–solid interfaces, so that in most of what follows medium 1 in (3.1) is fixed by the parameters of water, which are given in Table 1. For a given fluid, the behaviour of the interface modes can be greatly influenced by the (visco-)elastic properties of the solid, which we explore below. As is done in several works (e.g. [13]) in order to illustrate this, we will concentrate on two solids of opposing nature, namely steel and PVC whose values are also shown in Table 1. As we will showcase below, when compared to water these values correspond to hard/soft materials respectively (for both definitions presented above). Furthermore, in order to aid our study of the effect for the hard-soft transition on the relevant modes, we will make use of a linear continuous transition in all Material 2 parameters (listed in Tables 1, 2) through a function  $\mathbf{f} : [0, 1] \rightarrow \mathbb{R}^n$  s.t.

$$\mathbf{f}(\tau) = [\mathbf{Steel}](1 - \tau) + [\mathbf{PVC}](\tau) \quad 0 \leq \tau \leq 1, \quad (3.9)$$

where  $[\mathbf{Steel}]$ ,  $[\mathbf{PVC}]$  are simply vectors encoding all the physical parameters of each material. With regards to the frequency dependence of the VE moduli in the solid, we start by considering the KVM in Sections 3.3.1, 3.3.2 following (2.8a) for both the shear and bulk moduli, characterized by the viscosity coefficients  $\eta_\mu, \eta_K$  respectively. Consequently, the SLSM from (2.8a) is employed in Section 3.3.3, with further details provided there. For convenience, thermal effects are only illustrated with the KVM.

### 3.3 Modes at the interface of 2 semi-infinite half-spaces

Having defined the relevant equations to our physical set-up and material parameters in consideration, we now focus our attention to the solutions of the Stoneley DE (3.4), that can give rise to Leaky–Rayleigh and Stoneley–Scholte modes, which are considered individually next.

#### 3.3.1 The Leaky–Rayleigh (LR) Mode

We denote the LR mode solutions to (3.4), (3.7) by  $\bar{k}_{\text{LR}} = \bar{\omega}/\bar{c}_{\text{LR}}$ . It is well established that the LR wave propagates slightly slower than the associated solid’s shear body wave, marginally faster than the ordinary Rayleigh wave and attenuates in the direction of propagation due to part of the energy being shed into acoustic waves (radiated) into the fluid [11]. In most instances, this leakage is a consequence of the LR being *supersonic* ( $\text{Re}\{\bar{k}_{\text{LR}}\} < \text{Re}\{\bar{k}_{\text{F}}\}$ ). In fact, this was believed to be necessary for its existence (see e.g. [13]) prior to the work of [14], who showed the existence of subsonic leakage (although in a very small region) by careful analysis of the complex plane spectrum. Nevertheless, in most circumstances the LR cannot propagate and the inequality

( $\text{Re}\{\bar{k}_\Phi\} < \text{Re}\{\bar{k}_{\text{LR}}\} \leq \text{Re}\{\bar{k}_F\}$ ) usually holds. In practical conditions, the LR mode is also subject to an extra attenuating mechanism, namely that of visco-thermal boundary layer effects in the fluid, as well as the TVE damping within the solid. In [23] it was explicitly found that viscous effects dominate over heat conduction effects (especially for water) based on the original work [9], who first concluded that the effect of viscosity can be neglected for fluids with Reynolds number larger than 2500. We next showcase these differences by comparing solutions between the VE Stoneley DE, (3.4) with the inviscid fluid equivalent solution (3.7) as well as the TVE Stoneley DE (A.11).

Given the parameters in Table 1 and the discussion above, we note that for a water–PVC interface ( $\tau = 1$  in (3.9)) the LR cannot be supported, since the shear wave is highly subsonic ( $\text{Re}\{\bar{k}_F\} < \text{Re}\{\bar{k}_\Phi\}$ ), whereas for water–Steel ( $\tau = 0$  in (3.9)) the mode will exist. Starting from  $\tau = 0$ , as we transition through increasing  $\tau$  we observe the LR root becomes increasingly attenuative (per unit metre), until it reaches the subsonic region. A detailed analysis of the transition from the existence of the LR in the complex plane was provided in [14] via an isotropic gold-silver alloy with variable content in contact with water.

In order to numerically obtain the LR root using *fsolve*, as an initial guess we simply choose a real value that is slightly slower than the solid’s shear wave speed. Indeed, we obtain that the LR mode solution to (3.4) for Steel at 10 kHz gives  $\bar{k}_{\text{LR}} = 22.44 + 0.24i \text{ m}^{-1}$ , whereas for  $M_{\tau=0.9}$  (the artificial material corresponding to  $\tau = 0.9$  in (3.9)),  $\bar{k}_{\text{LR}} = 31.49 + 2.238i \text{ m}^{-1}$ , whose associated (normalized) horizontal particle displacements  $\text{Re}\{u_x\}$  are given in Figure 2 a),b),d) (all of which have been normalized such that  $u_x(y = x = 0) = 1$ ). We observe that the motion (and hence energy) of the LR is radiated as a pressure wave in the fluid propagating in the direction of the Rayleigh angle  $\theta_{\text{Ra}} = \arctan\{\text{Re}(i\bar{\gamma}_{\phi_1}) / \text{Re}(\bar{k}_{\text{LR}})\}$  which is measured anti-clockwise from  $x = 0$  (see Fig 2a)). For instance, water–steel gives  $\theta_{\text{Ra}} = 57.826^\circ$ , whereas for water– $M_{\tau=0.9}$   $\theta_{\text{Ra}} = 41.857^\circ$ . From the expanded Fig 2b) we observe the viscous boundary layer region in the fluid, which we remark is very thin (at 10 kHz we have approximately  $\bar{\delta}_\nu \approx 4 \mu\text{m}$ ). As with the traditional Rayleigh mode, the motion within the solid half-space is very localized near the boundary. The dissipation for increasing  $x$  parallel to  $y = 0$  is very apparent for  $M_{\tau=0.9}$ , where the motion in the solid in Fig 2d) cannot be appreciated due to the higher magnitude of the mode along the positive  $y$  direction (fluid region), as indicated by the colour bar.

When performing the same calculations as above but with the Scholte DE (3.7) (i.e. considering the inviscid fluid limit) we obtain very accurate answers for the phase speed and attenuation for both materials, despite the boundary layer effects observed for  $u_x$  naturally not being captured since in this case we are allowing the fluid to slip in the horizontal direction. On the other hand, the (VE) pure Rayleigh DE (3.6) in the absence of fluid loading predicts the phase velocity fairly accurately, but fails to account for the attenuation<sup>1</sup>, as shown in Fig 2c), from which we can conclude that energy radiation is indeed the predominant effect contributing to the attenuation of this mode, with boundary layers and the solid’s VE damping playing a much smaller role, which would be inconsequential in most practical scenarios. The result of thermal effects on the LR mode is included in Fig 2c), which we note gives a slightly higher phase speed as opposed to the isothermal equivalent. More generally, in Fig 2c) we also observe almost no dispersion (at the  $y$  scales provided) of the LR mode for  $M_{\tau=0.9}$  which we also found to be the case for steel, and tested it up to MHz frequencies.

<sup>1</sup>Particularly for  $M_{\tau=0.9}$ , which is in accordance with the observation noted just below (3.7) regarding the role of the density ratio  $\rho_s$ .

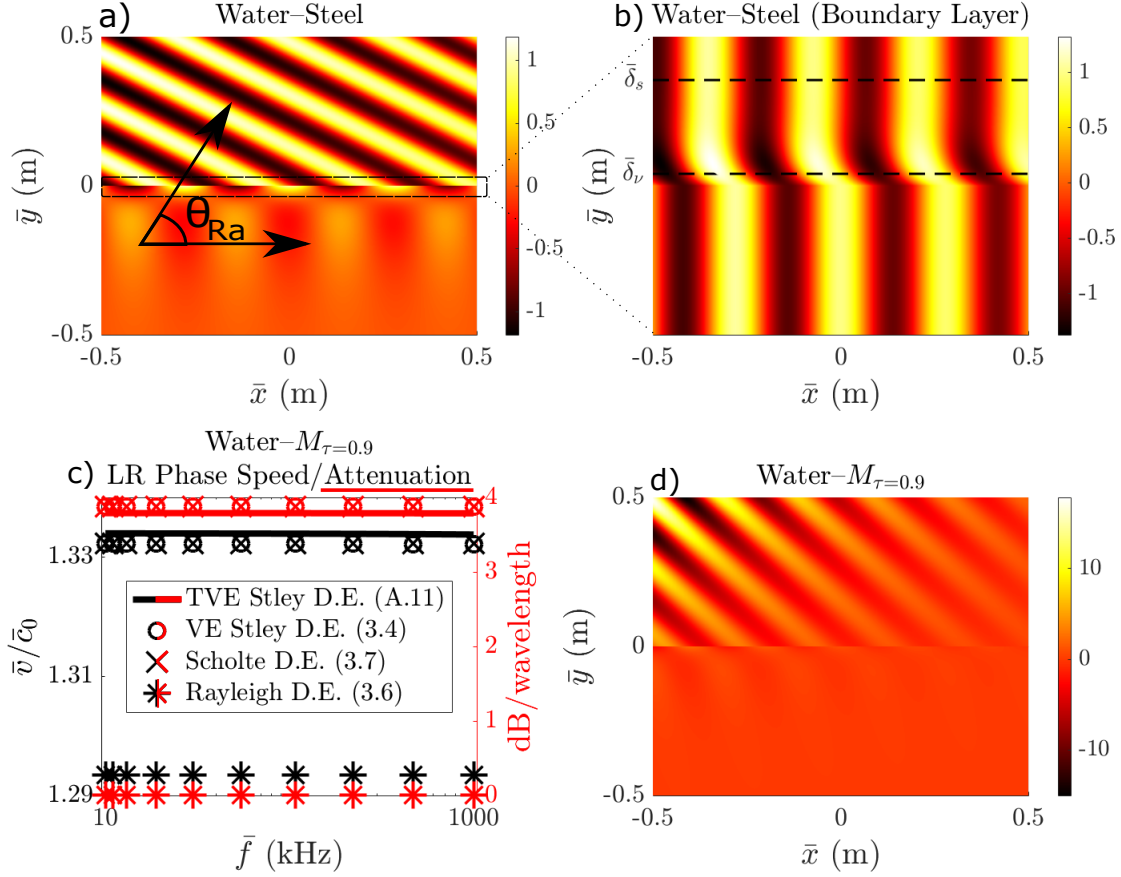


Figure 2: Heatmaps a), b), d) illustrate the dimensionless horizontal particle displacement  $\text{Re}\{u_x\}$  of the Leaky-Rayleigh mode from (3.4) at 10 kHz for water-steel (a), (b) and water- $M_{\tau=0.9}$  (d). (b) corresponds to the same calculation as (a) but near the boundary (as indicated by the small dotted lines) and all three plots have been normalized such that  $u_x(y = x = 0) = 1$ . In c) we give comparisons (in phase speed/attenuation) between the LR solutions obtained by different DEs for water- $M_{\tau=0.9}$ , noting the two different  $y$  scales represented by black/red.

### 3.3.2 The Scholte–Stoneley (Sc) Mode

We denote the Sc mode solutions to (3.4), (3.7), (A.11) by  $\bar{k}_{\text{Sc}} = \bar{\omega}/\bar{c}_{\text{Sc}}$ . The Stoneley–Scholte mode is an acoustic surface wave whose velocity is *subsonic* and slower than the bulk waves of the solid (i.e.  $\text{Re}\{\bar{k}_\phi\}, \text{Re}\{\bar{k}_\Phi\}, \text{Re}\{\bar{k}_F\} \leq \text{Re}\{\bar{k}_{\text{Sc}}\}$ ) and, when neglecting the thermo-viscous effects of both liquid and solid, it travels unattenuated along the interface, and decays exponentially away from it. Unlike the LR case above, it is present for all fluid–solid interfaces, although its behaviour is highly influenced by the material properties in question, as pointed out in [3]. Following Section 3.2, for a fixed fluid (in our case water), *soft* solids yield deeper penetration depths of the Sc mode and are therefore more convenient for applications [13]. With regards to losses in the fluid region, Stoneley–Scholte modes can be attenuated through two mechanisms, namely through boundary layer leakage of shear/vortical waves from the interface into the fluid, and through the longitudinal bulk waves in the thermo-viscous fluid. Nevertheless, for the latter to be noticeable the frequencies must be very high, and in general for both mechanisms to become important the viscosity of these fluids must be fairly high (e.g. in the experiments of [25] glycerol and honey are used). Indeed, [35], [10] concluded that for low viscosity fluids (including water), the effects on the Sc mode are such that it can generally be ignored. The VE effects within softer solids were studied theoretically and experimentally by Favretto-Anrès [12], [15] who found weak dispersion in the lower frequency range for synthetic resins in contact with water.

In this case, for the starting point for our DE solver, we choose a real valued  $\bar{k}$  whose real part is greater than  $\max(\text{Re}\{\bar{k}_F\}, \text{Re}\{\bar{k}_\Phi\})$ . We obtain that the Sc solution to (3.4) for Steel at 10 kHz gives  $\bar{k}_{\text{Sc}} = 42.163 + 1.3 \times 10^{-4}i \text{ m}^{-1}$  (noting that  $\bar{k}_F = 42.149 + 2.5 \times 10^{-6}i \text{ m}^{-1}$ ), for PVC  $\bar{k}_{\text{Sc}} = 70.70 + 0.0012i \text{ m}^{-1}$  whereas for  $M_{\tau=0.9}$  we obtained  $\bar{k}_{\text{Sc}} = 43.788 + 0.001i \text{ m}^{-1}$ . The difference in the real parts of these roots is remarkable, showing that this PVC is also soft according to the definition used in [3] (following the discussion from Section 3.2). Illustrations of these roots are presented in Figure 3. Unlike with the LR above, we can now observe the *trapped* nature of the mode (especially in Fig 3a)) propagating parallel to the  $y = 0$  interface. We nevertheless observe the aforementioned large differences in penetration depths between steel and PVC. With steel Fig 3d), the decay length in the water is long and the overall behaviour near the boundary resembles that of a longitudinal wave in the fluid at grazing incidence, whereas for PVC we observe much more motion distributed into the solid, and much shorter decay lengths in the fluid as seen in Fig 3a). Given the value of the roots, this can also be easily seen analytically by simply assessing the real part of the various square root functions (3.2) appearing in (3.1). Similar qualitative results in terms of energies are explicitly given in [12] and [3]. From Fig 3b) we can observe how the smaller acoustic impedance mismatch between water and PVC also results in a weaker boundary layer effect compared to that for water–steel (as shown for the LR in Fig 2b)).

As for the LR case, from Fig 3c) we again observe that the Scholte DE gives very accurate approximations (with respect to the VE Stoneley DE (3.4)) to both the phase speed and attenuation of the Sc mode. The differences in attenuation in Fig 3c) become more noticeable at higher frequencies, with the TVE and VE solutions behaving very similarly. Note, however the much smaller attenuation values observed for the Sc mode (compared to the LR) since in an ideal fluid–solid interface there is no dissipative mechanism and the root becomes purely real-valued. In Fig 3c) there is no notable dispersion in the phase speed of the Sc mode for water–PVC, and we find (not shown) that the same occurs for steel and  $M_{\tau=0.9}$  up to MHz frequencies. Similarly to the LR, including thermal effects predicts slightly higher phase speed values. Furthermore, so far we have only been considering the KVM such that e.g.  $\text{Im}\{\bar{\mu}(\bar{\omega})\} = -i\bar{\omega}\bar{\eta}_\mu$  (in both the fluid and solid, for a constant  $\bar{\eta}_\mu$ ) and therefore the larger  $\bar{\omega}\bar{\eta}_\mu$ , the higher values of dissipation, with the real part

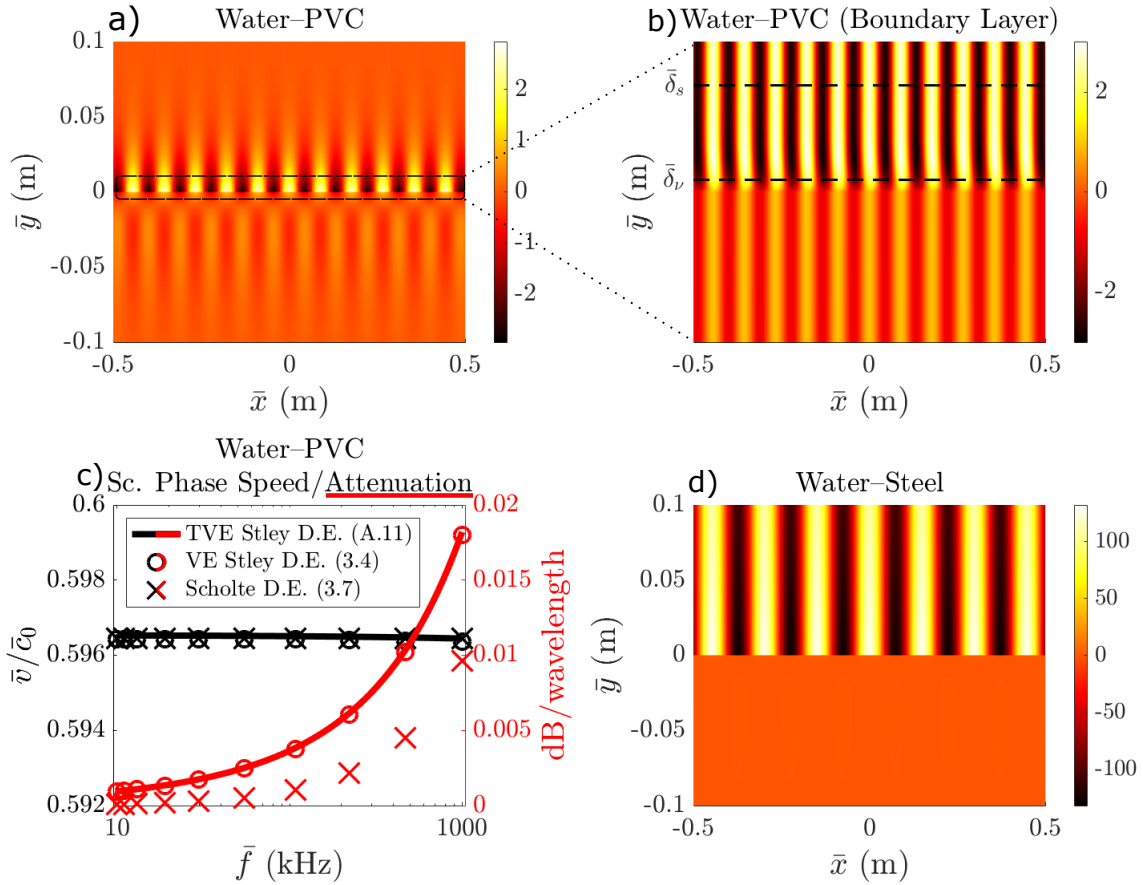


Figure 3: Heatmaps a), b), d) illustrate the dimensionless horizontal particle displacement  $\text{Re}\{u_x\}$  of the Scholte–Stoneley mode from (3.4) at 10 kHz for water–PVC (a), (b) and water–Steel (d). (b) corresponds to the same calculation as (a) but near the boundary (as indicated by the small dotted lines) and all three plots have been normalised such that  $u_x(y = x = 0) = 1$ . In c) we compare the phase speed and attenuation predicted by the TVE & VE Stoneley DEs (A.11), (3.4), and the Scholte approximation (3.7) for the water–PVC case, noting the two different  $y$  scales represented by black/red.

remaining constant. For the fluid this is often an accurate model since in this work we are focused on water [36], but this is not generally the case for softer solid media, particularly due to the importance of stress relaxation effects [1]. These are the main topic of discussion in the next section.

### 3.3.3 Additional frequency dependence: Influence of stress relaxation

As aforementioned, VE effects on the Sc mode for water–synthetic resins were analysed in [12], [15]. Despite the model used corresponding to a Kelvin–Voigt type model (for fixed frequency), they made acoustical measurements to obtain attenuation coefficients that can be related to viscosity via non-linear functions of frequency. In particular this means that in their case e.g.  $\bar{\eta}_\mu \equiv \bar{\eta}_\mu(\bar{\omega})$  (similarly with the bulk viscosity) which becomes a function that must be calculated at each individual frequency and is therefore not constant as in (2.8a). Furthermore, in their experiments it was found that body wave speeds were almost constant in the range 100 kHz–5 MHz, but they extended this range to cover lower frequencies in their study, so that the sound speeds (and hence the real part of the elastic moduli) are assumed constant in a wide range of frequencies ranging from 20 kHz–1 MHz. Despite these strong assumptions, they obtained accurate predictions of the Sc mode in a number

of different scenarios that were confirmed experimentally. In particular, they found low frequency (10 – 60 kHz) dispersion in the water–PVC interface which was not captured with the KVM with the parameters from Table 1, see Fig 3c).

In what follows, from a theoretical standpoint we want to include the frequency dependence of the bulk speeds of sound and draw particular attention to the effect of stress relaxation, which is generally most noticeable at lower frequencies [18]. Coincidentally, the importance of these effects were recently pointed out in [3], who noticed their appearance by experimentally extracting values of the Young’s modulus for acrylic using *coupled Scholte modes* (which we discuss in Section 4.4). Although an analysis of stress relaxation effects is not considered in [3], it is shown that for a given fluid, the Sc mode is almost independent of the solid’s Poisson ratio. More generally, weak frequency dependence of Poisson ratio in VE materials is often found in experiments [37]. We will therefore proceed by keeping  $\nu_2$  constant and letting the frequency dependence of the Young’s modulus  $\bar{E}_2(\omega)$  obey the SLSM (2.8b), that is, Material 2 satisfies

$$\nu_2(\omega) = \nu_2, \quad \bar{E}_2(\omega) = \bar{E}_\infty - (\bar{E}_0 - \bar{E}_\infty) \frac{i\omega t_r}{1 - i\omega t_r}, \quad (3.10)$$

noting that this assumption implies that the solid’s shear modulus  $\bar{\mu}_2(\omega)$  also satisfies the SLSM with the same relaxation time, and moduli  $\bar{\mu}_0, \bar{\mu}_\infty$  (see e.g. [38]). Prony series have shown to be very useful to model the relaxation behaviour of a wide number of VE materials [39]. With (3.10) we are employing the simplest case of Prony series by accommodating a single relaxation time  $t_r$ , which in practice is obtained by fitting the model to data from relaxation tests. Nevertheless, as discussed in [1], it is important to stress that for all real materials, a careful broadband experimental characterization will showcase frequency dependence in all material properties and ought to be taken into account for material-specific studies. Since we do not have easily accessible experimental data, here we will proceed with this assumption and analyze the behaviour resulting from different values of the relevant parameters. We want to observe how the phase speed/attenuation of the modes of propagation can vary according to these parameters and relate the results to those obtained above with local VE. We ignore thermal coupling in this section, although these can be directly incorporated into the DE (A.12) without any additional modelling considerations.

In Figure 4, we illustrate these effects by plotting the phase speed/attenuation for a particular example with parameters for Material 2

$$\text{a) } \bar{E}_0/\bar{E}_\infty = 1.12, \quad \nu_2 = 0.3528 \quad \text{b) } \nu_2 = 0.3528, \quad \omega t_r \in [0.01, 50] \quad \text{with 10 kHz,} \quad (3.11)$$

together with those for water (Material 1) in Table 1, where we have based the parameters around the PVC sample from Table 1 and assumed that they correspond to the rubbery phase of the material, such that  $\bar{E}_\infty = 4.4524$  GPa. In Fig 4a) we observe the phase speed and attenuation as a function of the relaxation time covering the range  $\omega t_r \in [0.01, 50]$ . We note an expected increase in velocity as the material transitions from rubbery to glassy, as well as a notable global maximum in attenuation close to  $\omega t_r = 1$  (although not exactly, due to the square root of the elastic moduli appearing in the wavenumbers). In order to obtain the value of this maximum with the KVM used above at 10 kHz, the shear viscosity coefficient of PVC in Table 1 would become as large as  $\bar{\eta}_{\mu_2} = 1500$  Pa·s, illustrating the large differences between the SLSM and KV formulations. In Fig 4b) we provide the maximum phase speed difference (which given our parameters from (3.11) is given by  $\max \Delta \bar{v} = \bar{v}_{\omega t_r=50} - \bar{v}_{\omega t_r=0.01}$ ) as well as the maximum value of attenuation for different ratios  $\bar{E}_0/\bar{E}_\infty$ . As expected, as this ratio increases the effects observed in Fig 4a) become largely enhanced, noting the larger difference in the attenuation maximum between the body waves and the Sc solution.

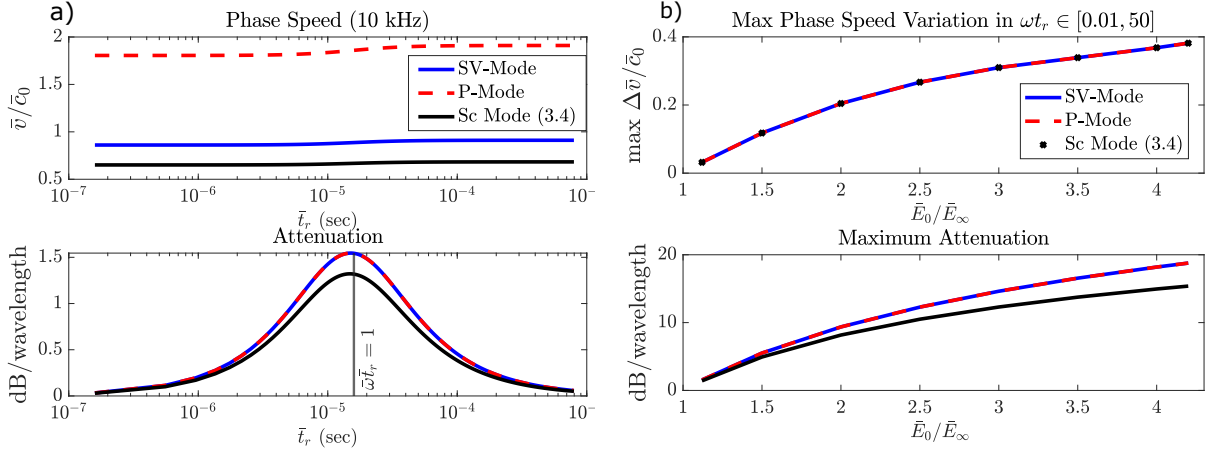


Figure 4: a) Relative phase speed/attenuation of the body and Sc modes following the SLSM at varying relaxation times. b) Maximum phase speed difference and maximum attenuation of the body and Sc modes following the SLSM for increasing values of the ratio  $\bar{E}_0/\bar{E}_\infty$ . Parameters are specified in (3.11). Note that the maximum attenuation in a) does not occur exactly at  $\omega t_r = 1$ , since the wavenumber is proportional to the square root of the moduli satisfying the SLSM.

These preliminary results illustrate the importance of the Deborah number and equivalently the frequency of operation and approximate relaxation time of the material in question which can cover several orders of magnitude e.g. for polyurethane (PU) it can vary between  $10 - 10^3$  (sec) [40], and therefore these effects would only be noticeable at extremely low frequencies. At higher frequencies (due to the small dispersion of the Sc mode in this regime, e.g. Fig 3c), [15]) for fixed material parameters, the behaviour resembles the situation in Fig 4a) with the  $x$  axis scaled accordingly.

So far we have only discussed these effects for the Sc mode (and body waves) since, as we saw above the PVC material from Table 1 could not support LR modes when in contact with water. Since this value is now being used as the rubbery phase of the Young's modulus, for a sufficiently large glassy phase ( $\bar{E}_0$ ) the LR should also become a solution. We illustrate this in Figure 5 with  $\bar{E}_0/\bar{E}_\infty = 4.043$ , where we give a wider range of relaxation times in the glassy phase of the material, namely  $\omega t_r \in [50, 5000]$ . The increase in phase speed is therefore almost unnoticeable, nevertheless we can clearly see the decrease in attenuation for the various modes at higher relaxation times. As we saw in Fig 2c) for  $M_{\tau=0.9}$ , the LR mode has a much higher attenuation due to energy radiation, so a separate scale is given in Fig 5 (on the right, in cyan) to represent its decrease. From a practical perspective, this also shows that stress relaxation effects can be noticed far away from glass transition, especially the larger the ratio  $\bar{E}_0/\bar{E}_\infty$  becomes.

It is worth remarking that the dispersive behaviour illustrated in Figures 4, 5 and discussed above requires a viscoelastic model that captures stress relaxation such as the SLSM employed here, as opposed to e.g. the standard KVM discussed earlier. Naturally, by using measurements to develop a frequency dissipation coefficient  $\bar{\eta}_\mu(\bar{\omega})$  as employed in [15] (rather than the constant  $\bar{\eta}_\mu$  in the standard KVM), the attenuative properties can be accurately predicted, however it cannot capture the changes in phase speed observed in the top figures of Fig 4a),b). Therefore, if the frequencies are sufficiently high this becomes a good approximation as seen from the top of Figure 5, but care must be taken in the lower frequency range, as discussed in e.g. [3] and [18].

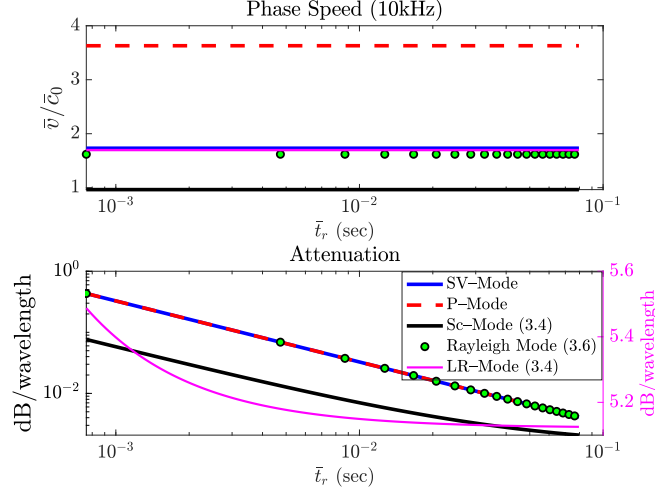


Figure 5: Relative phase speed/attenuation of various modes for the ratio  $\bar{E}_0/\bar{E}_\infty = 4.043$  covering the larger range  $\omega t_r \in [50, 5000]$  representing the stiffer phase of the material. The magenta  $y$  axis in the lower plot corresponds to the magenta curve only (i.e. the LR Mode from DE (3.4)).

## 4 Double interface: VE waveguides/plates bounded by semi-infinite VE continua

Having analysed the acoustic surface mode solutions to the initial single interface configuration consisting of two semi-infinite half-spaces in 2D, we next consider an additional parallel interface separated from the first interface by a distance of  $\bar{W} = 2\bar{L}$ , as shown in the right of Figure 1. Our framework will conveniently allow us to study the dissipative mechanisms in two physically different problems under the same set of dispersion equations, namely fluid-filled channels within solids and fluid-loaded plates; analysed in Sections 4.3, 4.4 respectively. The relevant DEs are discussed shortly, but it will be convenient to first non-dimensionalise the problem.

### 4.1 Non-dimensionalisation

Unlike in the case of a single interface, in the current geometry there is a clear length scale dictated by the finite dimension of Material 1. It is therefore convenient to non-dimensionalise the relevant equations, which we do via

$$\begin{aligned} \Delta &= \bar{L}^2 \bar{\Delta} \quad \omega = \frac{\bar{L}\bar{\omega}}{\bar{c}_\square}, \quad \{\mathbf{u}_m, \mathbf{x}\} = \frac{1}{\bar{L}}\{\bar{\mathbf{u}}_m, \bar{\mathbf{x}}\}, \quad \{\boldsymbol{\sigma}_m, \lambda_m, \mu_m, E_m, \mathcal{Q}\} = \frac{1}{\bar{\rho}_1 \bar{c}_\square^2} \{\bar{\boldsymbol{\sigma}}_m, \bar{\lambda}_m, \bar{\mu}_m, \bar{E}_m, \bar{\mathcal{Q}}\}, \\ \rho_s &= \frac{\bar{\rho}_2}{\bar{\rho}_1}, \quad \{k, k_{\phi_m}, k_{\Phi_m}, \gamma_{\phi_m}, \gamma_{\Phi_m}\} = \bar{L}\{\bar{k}, \bar{k}_{\phi_m}, \bar{k}_{\Phi_m}, \bar{\gamma}_{\phi_m}, \bar{\gamma}_{\Phi_m}\}, \quad \{c, c_{\phi_m}, c_{\Phi_m}\} = \frac{1}{\bar{c}_\square} \{\bar{c}, \bar{c}_{\phi_m}, \bar{c}_{\Phi_m}\}, \\ t_r &= \bar{c}_\square \bar{t}_r / \bar{L}, \quad \{\phi_m, \Phi_m\} = \frac{1}{\bar{L}^2} \{\bar{\phi}_m, \bar{\Phi}_m\}, \quad \{\eta_{\mu_m}, \eta_{K_m}\} = \frac{1}{\bar{\rho}_1 \bar{c}_\square \bar{L}} \{\bar{\eta}_{\mu_m}, \bar{\eta}_{K_m}\}, \end{aligned}$$

where  $m = 1, 2$ . The (constant) sound speed ( $\bar{c}_\square$ ) will be chosen accordingly in Sections 4.3, 4.4.

## 4.2 The generalised dispersion equations

We set up the 2D coordinate system such that the  $x$  direction is aligned with the interfaces and  $y = 0$  lies in the middle of Medium 1, and we therefore must ensure that the continuity of traction and displacement boundary conditions (3.3) are satisfied at  $y = \pm 1$ . By exploiting the symmetry of the configuration about  $y = 0$ , the general  $8 \times 8$  system arising from the continuity BCs on each interface can be split into two independent  $4 \times 4$  systems (see e.g. [20]). Indeed, *symmetric modes* require  $u_x^1$ ,  $\phi_1$  to be even functions of  $y$  whereas  $u_y^1$ ,  $\Phi_1$  must be odd functions of  $y$ , therefore the potentials in (2.5) are given by

$$\phi_1 = P1_S \cosh(\gamma_{\phi_1} y) e^{ikx}, \quad \phi_2(x, y) = \begin{cases} P2_S e^{\gamma_{\phi_2}(y+1)+ikx}, & y \leq -1 \\ P2_S e^{-\gamma_{\phi_2}(y-1)+ikx}, & y \geq 1 \end{cases}, \quad (4.1a)$$

$$\Phi_1 = S1_S \sinh(\gamma_{\Phi_1} y) e^{ikx}, \quad \Phi_2(x, y) = \begin{cases} S2_S e^{\gamma_{\Phi_2}(y+1)+ikx}, & y \leq -1 \\ S2_S e^{-\gamma_{\Phi_2}(y-1)+ikx}, & y \geq 1 \end{cases}, \quad (4.1b)$$

for some complex valued amplitudes  $P1_S, P2_S, S1_S, S2_S$ . Given (4.1), it can be shown that symmetric modes are given by solutions to

$$\begin{aligned} & c^4 \left( (1 - \rho_s)^2 \tanh(\gamma_{\Phi_1}) - A_1 \rho_s \tanh(\gamma_{\phi_1}) (B_2 \tanh(\gamma_{\Phi_1}) + B_1 \rho_s) - A_2 B_2 \tanh(\gamma_{\Phi_1}) - A_2 B_1 \rho_s \right) \\ & + 2c^2 \mathcal{Q} (-\rho_s A_1 B_1 \tanh(\gamma_{\phi_1}) + (A_2 B_2 - 1 + \rho_s) \tanh(\gamma_{\Phi_1})) \\ & + \mathcal{Q}^2 (A_1 B_1 \tanh(\gamma_{\phi_1}) - \tanh(\gamma_{\Phi_1})) (A_2 B_2 - 1) = 0, \end{aligned} \quad (4.2)$$

which was derived in Mathematica, recalling that the quantities  $A_1, A_2, B_1, B_2, \mathcal{Q}$  are defined in (3.5) (and noting the non-dimensionalisation above). Conversely, *anti-symmetric modes* require  $u_x^1$ ,  $\phi_1$  to be odd functions of  $y$  and  $u_y^1$ ,  $\Phi_1$  to be even, such that

$$\phi_1 = P1_A \sinh(\gamma_{\phi_1} y) e^{ikx}, \quad \phi_2(x, y) = \begin{cases} -P2_A e^{\gamma_{\phi_2}(y+1)+ikx}, & y \leq -1 \\ P2_A e^{-\gamma_{\phi_2}(y-1)+ikx}, & y \geq 1 \end{cases}, \quad (4.3a)$$

$$\Phi_1 = S1_A \cosh(\gamma_{\Phi_1} y) e^{ikx}, \quad \Phi_2(x, y) = \begin{cases} S2_A e^{\gamma_{\Phi_2}(y+1)+ikx}, & y \leq -1 \\ S2_A e^{-\gamma_{\Phi_2}(y-1)+ikx}, & y \geq 1 \end{cases}, \quad (4.3b)$$

for complex valued amplitudes  $P1_A, P2_A, S1_A, S2_A$ . Similarly, given (4.3) it can be shown that anti-symmetric modes are given by solutions to

$$\begin{aligned} & c^4 \left( (1 - \rho_s)^2 \tanh(\gamma_{\phi_1}) - B_1 \rho_s \tanh(\gamma_{\Phi_1}) (A_2 \tanh(\gamma_{\phi_1}) + A_1 \rho_s) - A_2 B_2 \tanh(\gamma_{\phi_1}) - A_1 B_2 \rho_s \right) \\ & + 2c^2 \mathcal{Q} (-\rho_s A_1 B_1 \tanh(\gamma_{\Phi_1}) + (A_2 B_2 - 1 + \rho_s) \tanh(\gamma_{\phi_1})) \\ & + \mathcal{Q}^2 (A_1 B_1 \tanh(\gamma_{\Phi_1}) - \tanh(\gamma_{\phi_1})) (A_2 B_2 - 1) = 0, \end{aligned} \quad (4.4)$$

and it is straightforward to check that in the short-wavelength limit  $\gamma_{\phi_1}, \gamma_{\Phi_1} \gg 1$  both (4.2), (4.4) recover the Stoneley DE (3.4) (since in this limit there is no distinction between symmetric and anti-symmetric motion). This natural geometric consequence will allow us to use the knowledge of the two semi-infinite half-space configuration discussed in Section 3 in order to obtain the initial behaviour within the slit/plate. We show in Appendix A.3 that when thermal effects are present, (4.2), (4.4) take the more general forms (A.15), (A.17) which require taking the determinant of  $6 \times 6$  matrices. Having obtained the general dispersion equations for natural modes of interest (4.2), (4.4), we will next focus on the analysis of the two distinct limits of physical interest here.

### 4.3 Limit A): Fluid-filled channels within semi-infinite solids

As aforementioned, the effects of visco-thermal boundary layers and FSI in narrow water/air-filled slits were examined extensively in [2]. In the FSI analysis therein, the only solid material considered was steel, which given the discussion above constitutes a hard solid when in contact with water (for air, in all cases FSI effects were negligible). In this section, we explore the differences arising when soft TVE media are instead considered.

Following [2], the analysis below is focused only on the lowest order symmetric mode, so that here we will only be considering the roots of (4.2). The rationale employed in [2] was that this was sensible since for an inviscid fluid with rigid BCs it is the only propagating mode at our region of interest; namely thin channel widths/low frequencies. Of course, FSI effects arising from the consideration of solid media in contact with water are such that the rigid BC does not apply, and the current situation is far from this idealized scenario, since we are also analysing softer solid media. Nevertheless, the main objective of this section is to extend the results presented in [2] by including the effects of TVE losses within the (infinite) solid bounding the fluid, together with the previously considered boundary layer effects.

As we will see shortly, the mode in consideration is in fact strongly related to the Sc mode from Section 3.3.2, which becomes coupled in the slit region as the thickness decreases (with respect to the transverse wavelength). As a result, we are essentially studying the ‘coupled duct–Scholte mode’ including dissipation. On the other hand, unlike for the half-space, geometrical confinement implies that LR waves cannot radiate energy away from the interfaces and hence propagate plane-wave like with little attenuation along the channel. Therefore, as opposed to the coupled duct–Scholte mode, they are only expected to propagate in sufficiently wide channels [2].

Given the non-dimensionalisation in Section 4.1, in this Section we let  $\bar{c}_\square \equiv \bar{c}_0 = 1490$  m/s i.e. we choose the adiabatic speed of sound in water at 10 degrees Celsius and  $\bar{\rho}_1 = 1000$  kg/m<sup>3</sup> (following Table 1). With regards to the choice of VE frequency dependence, we will follow a similar structure to Section 3 for the single interface: first we assume the KVM for the solid according to Table 1, and then we consider the SLSM in Section 4.3.3.

#### 4.3.1 Phase speed and attenuation

In order to find the roots of (4.2) using *fsolve*, we make use of an iterative numerical scheme, whose starting point is dictated by the solutions to the Stoneley DE (3.4), corresponding to the wide channel limit, as noted just below (4.4) (similarly for the case when thermal coupling is considered; to find the roots of (A.15), the starting point is dictated by the solutions to (A.11)). We subsequently gradually reduce the channel widths up to the values of interest, by using the root found for the prior larger value of  $\bar{W}$  as a new starting point for *fsolve*. In Figure 6 we observe the phase speed/attenuation as a function of channel width in terms of  $\bar{\delta}_s/\bar{W}$  at 10 kHz for a) water–steel and b) water–PVC. We directly observe the difference in phase speed between the hard/soft solids at wide channel widths. In particular, the mode in water–PVC is highly subsonic, as we observed in Fig 3c) for the half-space Sc mode. More generally, it is clear that FSI effects in both materials dramatically reduce the phase speed along the channel as opposed to the rigid case. We observe that for the parameters used in Figs 6 a),b), phase speed and attenuation among the thermo-viscous fluid–TVE interface (red curves) remains almost identical to the viscous fluid–VE results (black dashed curves). The rigid BC results (cyan curve) where the solid motion is ignored is plotted for reference. For further comparisons we give additional curves that neglect particular physical effects. In particular, for the inviscid fluid we assume medium 1 is s.t.  $\mu_1(\omega) \rightarrow 0$ , implying that  $k_{\Phi_1}^2 \rightarrow \infty$  and hence

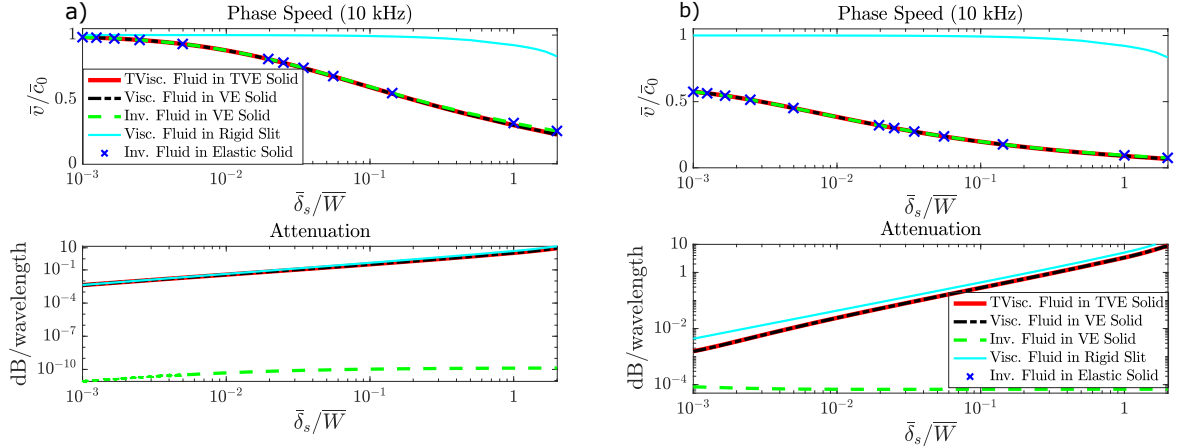


Figure 6: Phase Speed/Attenuation at 10 kHz for water-filled channels of decreasing width within semi-infinite a) Steel, and b) PVC media, according to the KVM with material properties in Table 1 (and Table 2 for the red curves). In particular, we note the large difference in the initial value of the phase speed between a) and b) which is dictated by the Stoneley DE (3.4).

$\gamma_{\Phi_1}, B_1 \rightarrow \infty$  whereas  $\mathcal{Q} \rightarrow -2\rho_s c_{\Phi_2}^2$  and (4.2) simplifies to

$$\tanh(\gamma_{\phi_1}) [(2k^2 - k_{\Phi_2}^2)^2 - 4k^2 \gamma_{\phi_2} \gamma_{\Phi_2}] + \frac{\gamma_{\phi_2} k_{\Phi_2}^4}{\gamma_{\phi_1} \rho_s} = 0, \quad (4.5)$$

noting the similarity with the limit taken to arrive at the Scholte DE (3.7) from the Stoneley DE (3.4) in the half-space configuration. Equation (4.5) is identical to equation (72) in [2] except here in the parameters for medium 2 we are including frequency dependence (barring the blue crosses in Figures 6, 7 where we further let  $\eta_{\mu_2}, \eta_{K_2} \equiv 0$  in the solid which yields real valued roots). Nevertheless, the VE losses in both solids remain small, as can be seen from the green curves in the bottom plots from Fig 6, which shows that the great majority of the attenuation is indeed due to the boundary layers in water (red/black curves). Note that this is expected for steel at these frequencies due to its negligible viscosity, but less so for PVC (Table 1). When performing similar calculations at higher frequencies, we find that the phase speed values for most (fixed) channel widths become larger, whilst the attenuation remains fairly constant. This is shown explicitly for water-PVC in Figure 7a) for the particular case when  $\bar{\delta}_s/\bar{W} = 0.5$ , noting that a similar frequency dependence is obtained for steel in [2]. Dispersion in attenuation can nevertheless be seen when a higher coefficient of viscosity is employed, as illustrated in Figure 7b) where we used  $\bar{\eta}_{\mu_2} = 10$  Pa·s, although it has close to no effect on the relative phase speed. Finally, following our initial discussion above, we can only observe the coupled LR-duct mode for water-steel at 10 kHz up to  $\bar{\delta}_s/\bar{W} \approx 0.03$ ; for thinner channels it becomes cut-off (not shown).

#### 4.3.2 Displacement fields

The particle motion of the mode under consideration for a water-steel interface was studied in detail in [2]. Here we simply want to illustrate whether any significant changes occur when steel is replaced by a softer medium. In Figure 8 we give direct comparisons between steel/PVC of the horizontal displacement  $\text{Re}\{u_x\}$  for a wide channel, represented by  $\bar{W} = 70\bar{\delta}_s$ . The behaviour in the

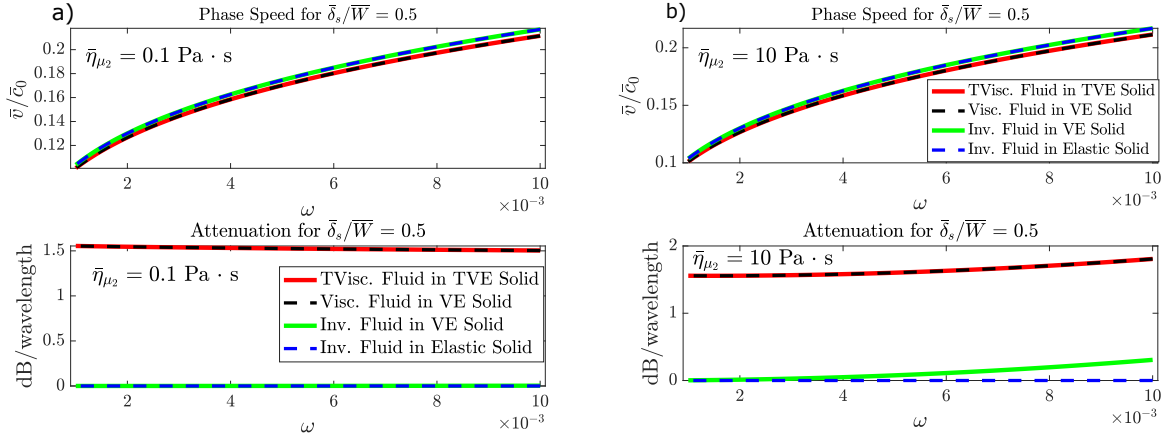


Figure 7: Relative phase speed/attenuation at fixed channel width  $\bar{\delta}_s/\bar{W} = 0.5$  for increasing frequency in a water-filled PVC channel following the KVM for: a) Shear PVC viscosity coefficient  $\eta_{\mu_2}$  from Table 1, b) Larger shear PVC viscosity coefficient. In a) we observe dispersion in phase speed, but not in attenuation, whereas in b) we observe an additional VE frequency dependence in attenuation.

fluid region, Fig 8a),b) is rather similar between the two interfaces, noting that the boundary layer region is well approximated by Stokes' boundary layer  $\bar{\delta}_s/\bar{L}$ . Nevertheless, in Fig 8a) we also observe a slight decay from the boundary region towards the centre of the channel for PVC which is not observed in steel. We observe (not shown) that this feature becomes increasingly noticeable at wider channel widths. This is expected, since as the channel width becomes larger, the solution begins to resemble that of the half-space Sc mode localized in each boundary, and as we observed above, the decay length in the fluid is much longer for hard solids (Fig 3d)) than it is for softer media (Fig 3a)). On the other hand, in the solid region Fig 8c), we see a large difference between the motion in PVC and steel, with the displacement of the former being more than an order of magnitude larger than the latter at the interface  $y = \pm 1$ . Nevertheless, this motion still decays rapidly within the solid, which is expected since we observed in Figure 6b) that there was no damping due to radiation loss in the form of elastic waves through the interfaces into the solid. At narrower channel widths (not shown) the motion at the interface with the solid region becomes increasingly reduced, although the difference between hard/solid can still be appreciated.

#### 4.3.3 Additional frequency dependence: Influence of stress relaxation

As was done for the half-space, we now wish to assess whether the inclusion of stress relaxation effects via the SLSM in the *host* solid medium can alter the phase speed/attenuation of the Sc-duct mode under consideration. We observed in Figure 7 how, when employing the KVM with sufficiently high viscosity coefficient, the attenuation increases (unboundedly) with  $\omega$ , but this has no effect on the corresponding relative phase speed. We will follow the assumptions from Section 3.3.3 and assume a constant Poisson's ratio and let the Young's modulus (of Medium 2) obey the SLSM as in (3.10), noting that under the current non-dimensionalization the relaxation time is given by  $t_r = \bar{c}_0 \bar{t}_r / \bar{L}$ . As for the half-space, we do not discuss thermal coupling in this section.

For the illustrations, again we assume that the rubbery phase of the PVC material corre-

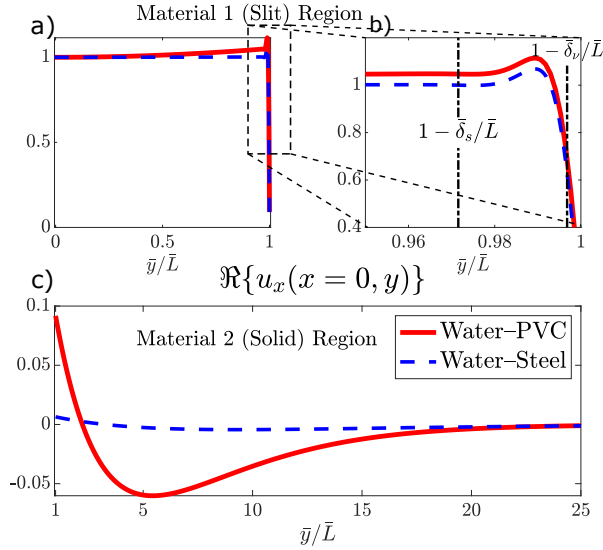


Figure 8: Real part of the horizontal displacement fields  $\Re\{u_x(x=0, y)\}$  for the lowest order symmetric mode propagating in a viscous water-filled channel at 100 kHz within steel/PVC, for a channel width of  $\bar{W} = 70\bar{\delta}_s$ . a) represents the fluid region  $0 \leq \bar{y} \leq \bar{L}$ , b) the fluid behaviour near the boundary, and c) the solid region  $\bar{L} \leq \bar{y} \leq 25\bar{L}$ . In each case the plots have been normalized such that  $u_x(y=x=0) = 1$ .

sponds to the value given in Table 1, so that  $\bar{E}_\infty = 4.4524$  GPa. In Figure 9 we give the phase speed/attenuation at various frequencies and channel widths as a function of relaxation time  $t_r$ , chosen in each case so that the range  $\omega t_r \in [0.01, 50]$  is covered, and therefore the glass transition of the material is showcased. The qualitative behaviour is therefore very similar within Figures 9a)–d), where we note the increasing phase speeds as the material becomes glassier, and the global maximum attenuation near  $\omega t_r = 1$ , as we saw in Figure 4a) for the half-space. Nevertheless, in this case there are significant changes in the relevant values when the main parameters vary, following what we saw in Figures 6, 7. That is, with higher frequencies (smaller channel widths) we observe overall higher values in phase speed, and the effect of the fluid’s viscosity becomes particularly relevant at narrower channel widths. Furthermore, as we observed for the half-space in Figure 4b), the larger the ratio  $\bar{E}_0/\bar{E}_\infty$  gets, the larger the maximum phase speed variation and maximum attenuation becomes.

In Figure 10 we give similar plots to those in Figs 6, 7 for various fixed relaxation times. In Figure 10a) the chosen  $t_r$  are such that  $\omega t_r = 0.1, 1, 50$  at the initial value of frequency, so that at this (initial) frequency we are covering the rubbery/glassy phases and glass transition. As a result, we observe how as frequency increases the attenuation of the initially rubbery phase ( $t_r = 100$ ) undergoes glass transition, whereas naturally in the two other cases ( $t_r = 1000, 50000$ ) an increase of frequency results in a reduction of attenuation (per wavelength). From Figure 10b) we observe how the initial phase speed is higher in the glassy phase, and particularly how with  $\omega t_r$  fixed, VE relaxation effects together with boundary layers can lead to a significant increase in attenuation (compared to e.g. Fig 6b)). Note that the small decrease in attenuation observed for wide channels in Fig 10b) occurs since we are plotting attenuation per wavelength (following (3.8b)) and is therefore caused due to the sharp decrease in phase speed observed in this region. Moreover, it is physically

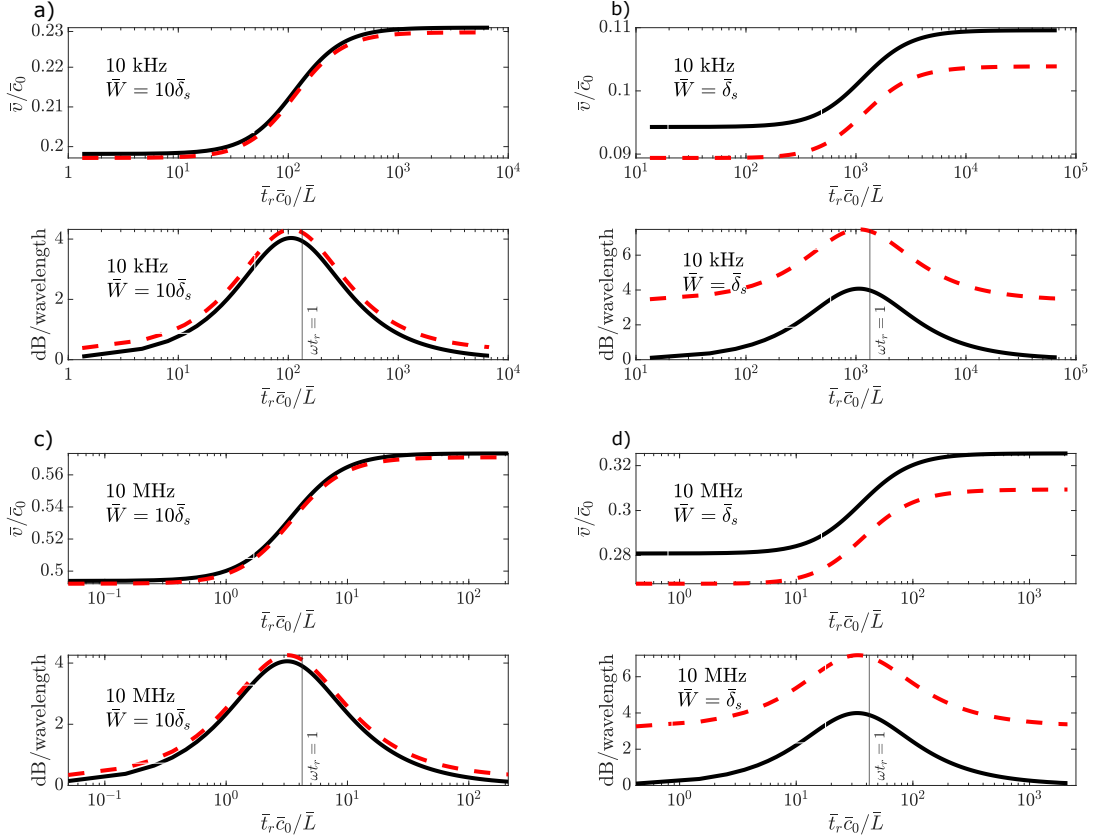


Figure 9: Relative phase speed/attenuation in a water-filled PVC slit obeying the SLSM, as a function of non-dimensional relaxation time  $t_r$  for various channel widths and frequencies. The red-dashed curve represents viscous water given by (4.2), whereas the black curve is for inviscid water and is therefore a solution to (4.5). In all cases we have  $\bar{E}_0/\bar{E}_\infty = 1.572$ , and the relaxation times chosen cover the range  $\omega t_r \in [0.01, 50]$ .

useful to also have an idea of this quantity along a fixed distance. In Figure 11 we plot attenuation per unit metre (given by  $20 \text{Im}(k) \log_{10}(e)$ ) as a function of channel width, and give differences between the viscous/inviscid fluid cases from (4.2), (4.5) respectively at different values of the Deborah number. In particular, we observe how for narrower slits, the large reduction in phase speed observed above results in shorter wavelengths and consequently higher attenuation per unit metre.

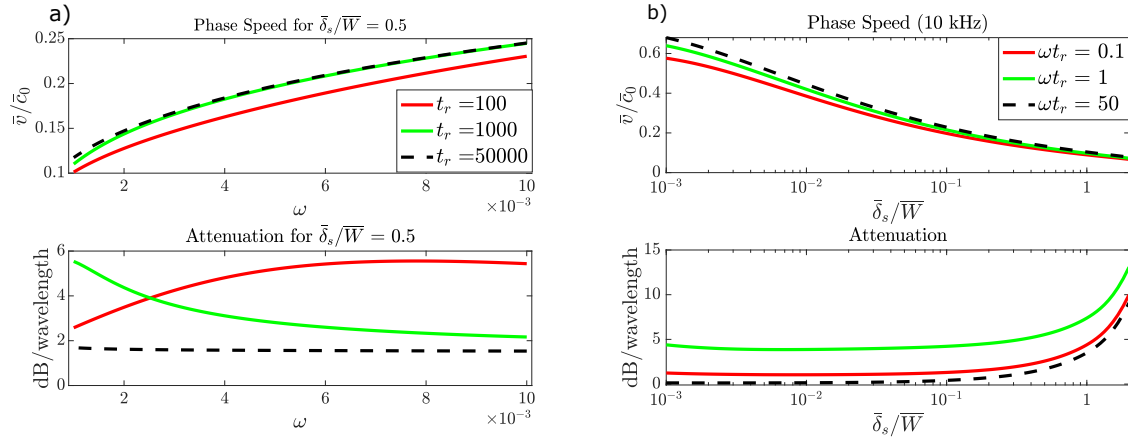


Figure 10: Relative phase speed/attenuation in a (viscous) water-filled PVC slit obeying the SLSM, with  $\bar{E}_0/\bar{E}_\infty = 1.572$ : a) as a function of frequency for a fixed channel width of  $\bar{\delta}_s/\bar{W} = 0.5$ , b) as a function of channel width with dimensional frequency 10 kHz. In each case the relaxation times have been chosen to represent the differences between the glassy/rubbery phases of the solid medium, noting the differences in attenuation in a) for the smaller relaxation times as the frequency increases.

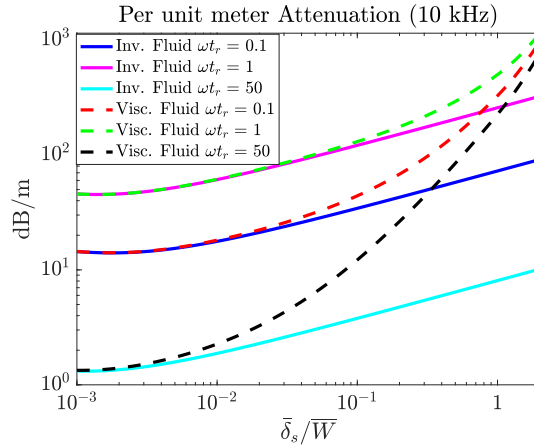


Figure 11: Attenuation per unit metre in a water-filled PVC slit obeying the SLSM, with  $\bar{E}_0/\bar{E}_\infty = 1.572$ . In each case the relaxation times have been chosen to represent the differences between the glassy/rubbery phases of the solid medium. Viscous (Visc.) fluid solutions are obtained from (4.2), whereas the inviscid (Inv.) fluid solutions are from (4.5).

## 4.4 Limit B): Fluid-loaded plates

We now want to explore the reciprocal situation to that just seen above, namely, Medium 1 in the right of Figure 1 now corresponds to a solid, whereas Medium 2 is a fluid (water), so that we have fluid-loaded plates. Much like for the half-space, in certain scenarios (hard interfaces) the fluid loading simply acts as a small perturbation to the traditional Lamb DEs for natural modes on a plate in vacuum (i.e. stress-free). In these cases the consideration of fluid loading causes the (pure) Lamb mode solutions to become leaky as some of their energy gets shed via radiation of acoustic waves in the fluid, and therefore the resulting modes are commonly addressed as ‘Leaky–Lamb’ modes in the literature, which have been widely studied including the effect of boundary layer losses e.g. [22, 24, 41].

However, the presence of Material 2 (here a fluid) gives rise to an additional set of solutions of a similar nature to the half-space Scholte–Stoneley addressed in Section 3.3.2. Naturally, the difference here is that for thin plates (compared to wavelength) these Sc type surface modes become interacting within the plate region and form two coupled interface modes, which are therefore the symmetric/anti-symmetric ‘coupled plate–Scholte’ modes, which we will refer to as ‘coupled–Scholte’ for brevity following [3]. For hard fluid–plate interfaces, the symmetric mode is often ignored since it is non-dispersive and lies on top of the sound line, and therefore the term ‘quasi–Scholte’ mode is often found in the literature to refer only to the anti-symmetric (e.g. [25]). The situation is nevertheless very different for soft interfaces, and in particular the symmetric coupled Sc can become highly dispersive, deviating from the Sc and fluid velocities, as recently confirmed experimentally in [3].

Following the same structure that we have employed in the preceding sections, here we want to emphasise the extra physical insights that our framework provides for the behaviour of coupled Sc modes. That is, the effects of the thermo-viscous boundary layers on either side of the plate as well as the TVE of the plate itself, particularly when stress relaxation is considered.

Given the non-dimensionalisation in Section 4.1, in this limit we let  $\bar{c}_\square \equiv \bar{c}_s$  i.e. we choose the lossless shear speed of sound in each solid material as appropriate (for steel  $\bar{c}_s = 3000$  m/s, and for PVC  $\bar{c}_s = 1100$  m/s) and similarly for the mass density (for steel  $\bar{\rho}_1 = 7871$  kg/m<sup>3</sup>, and for PVC  $\bar{\rho}_1 = 1360$  kg/m<sup>3</sup>). With regards to the choice of VE frequency dependence, we will follow a similar structure to what was done in the preceding sections: first we assume the KVM for the solid according to Table 1, and then we consider the SLSM in Section 4.4.3.

### 4.4.1 Phase speed and attenuation

By the equivalence of the DEs in consideration, in order to find the roots of (4.2), (4.4) using *fsolve*, we can make use of the same iterative procedure used for the slit, as explained in Section 4.3.1 so that the initial value in the thick plate limit relies on the roots of (3.4). Similarly, when thermal effects are considered, for the initial roots of the corresponding DEs (A.15), (A.17) we focus on the thick plate limit, given by the TVE Stoneley DE (A.11). As we have been doing thus far, in order to study the influence of the fluid viscosity, it is convenient to consider the inviscid limit such that  $\mu_2(\omega) \rightarrow 0$ , from which it follows that  $k_{\Phi_2}^2 \rightarrow \infty$  and hence  $\gamma_{\Phi_2}, B_2 \rightarrow \infty$  whereas  $\mathcal{Q} \rightarrow 2c_{\Phi_1}^2$  so that (4.2), (4.4) become

$$\left[ (2k^2 - k_{\Phi_1}^2)^2 \coth(\gamma_{\phi_1}) - 4k^2 \gamma_{\phi_1} \gamma_{\Phi_1} \coth(\gamma_{\Phi_1}) \right] + \rho_s \frac{\gamma_{\phi_1} k_{\Phi_1}^4}{\gamma_{\phi_2}} = 0, \quad (4.6a)$$

$$\left[ (2k^2 - k_{\Phi_1}^2)^2 \tanh(\gamma_{\phi_1}) - 4k^2 \gamma_{\phi_1} \gamma_{\Phi_1} \tanh(\gamma_{\Phi_1}) \right] + \rho_s \frac{\gamma_{\phi_1} k_{\Phi_1}^4}{\gamma_{\phi_2}} = 0. \quad (4.6b)$$

for symmetric and anti-symmetric modes respectively, which we will both be considering in this section. From (4.6), we observe explicitly that the terms in square brackets correspond to the classical Lamb DEs for modes on a free plate (in the absence of any loading  $\rho_s = 0$ ), where the VE effects are captured through the frequency varying material parameters appearing in the wavenumbers. The role of the density ratio  $\rho_s$  is analogous to (3.7) for the half-space. For  $\rho_s \ll 1$  we can see why (4.6) can be treated as a small perturbation to the stress-free Lamb DEs [42], nevertheless as the fluid density approaches that of the solid  $\rho_s \rightarrow 1$ , the similarities between the spectra can disappear completely [41].

In Figure 12 we give the relative phase speed/attenuation as a function of the plate thickness in terms of  $\bar{\delta}_s/\bar{W}$  at 10 kHz for: (a) water–steel, and (b) water–PVC. In both cases we observe how, in the thin plate (low frequency) limit the anti-symmetric mode tends to zero, whereas the symmetric mode tends to the fluid’s sound speed. Conversely in the thick plate (high frequency) limit, the two curves converge to the Stoneley–Scholte value. These observations are in agreement with the analysis in [20] and the dispersion curves in [3]. In terms of attenuation, we first notice the significantly smaller magnitude compared to those in the slit e.g. Figure 6, which is expected, since here the boundary layers are located on either side exterior to the plate, and are therefore never interacting (which is the regime with major viscous losses as observed in the preceding slit section). Furthermore, it is also apparent from the low attenuation values that the TVE effects of the plates, with the values used, have small impact. Given this, we nevertheless observe how the viscous boundary layer increases the attenuation of the anti-symmetric mode as the plate becomes thinner in both cases, with a small albeit notable distinction between the TVE and VE solutions as we approach  $\bar{W} = \bar{\delta}_s$  in both solids Figs 12a),b). The general increase in attenuation does not occur for the symmetric mode but instead, we observe a local maximum for water–PVC Figure 12b) around  $\bar{\delta}_s/\bar{W} \approx 10^{-3}$  which occurs near (but not exactly) the inflection point observed in the mode’s phase speed, but is not observed for steel since the symmetric mode’s speed remains constant Figure 12a).

In order to further analyse the dispersion of these modes, in Figure 13 we give an equivalent plot but increase frequency  $\omega$  by an order of magnitude (to 100 kHz) and superimpose (in grey) the TVE results from Figure 12 for ease of comparisons. We observe how this results in the separation of the phase speeds (between the symmetric and anti-symmetric modes) at thinner plate thicknesses and correspondingly so does the maximum attenuation of the viscous symmetric mode for PVC in Fig 13b) which also increases in magnitude as to be expected. In general, we observe that the inviscid fluid solutions obtained from (4.6) have an excellent agreement in phase speed with the full viscous solutions, but naturally cannot predict the attenuation due to the boundary layers.

#### 4.4.2 Displacement fields

The energy density associated with the coupled Sc mode for hard/soft plates of various thicknesses was analysed respectively in [25, 3], so here we will focus on the mode’s displacement fields. In Figure 14 we show heatmaps of (the real part of) the horizontal/vertical particle displacements fields for the symmetric coupled Sc mode in a PVC plate (Table 1) loaded with water at 10 kHz for a plate thickness of  $\bar{\delta}_s/\bar{W} = 10^{-3}$  (see Figure 12b) for reference). From the colorbars we note that the predominant motion is actually parallel to the interface (Figure 14a)) with significant motion coupled in both the plate and near the interface in the fluid. The anti-symmetric mode is given in Figure 15, noting that in this case the magnitude of the motion is much more distributed in both directions, with the predominant motion in the plate being perpendicular to the interface which is expected due to the ‘bending’ nature of the anti-symmetric mode. Note that, for this plot we have used a much thinner plate of  $\bar{\delta}_s/\bar{W} = 0.2$  in order to further illustrate the viscous boundary layers

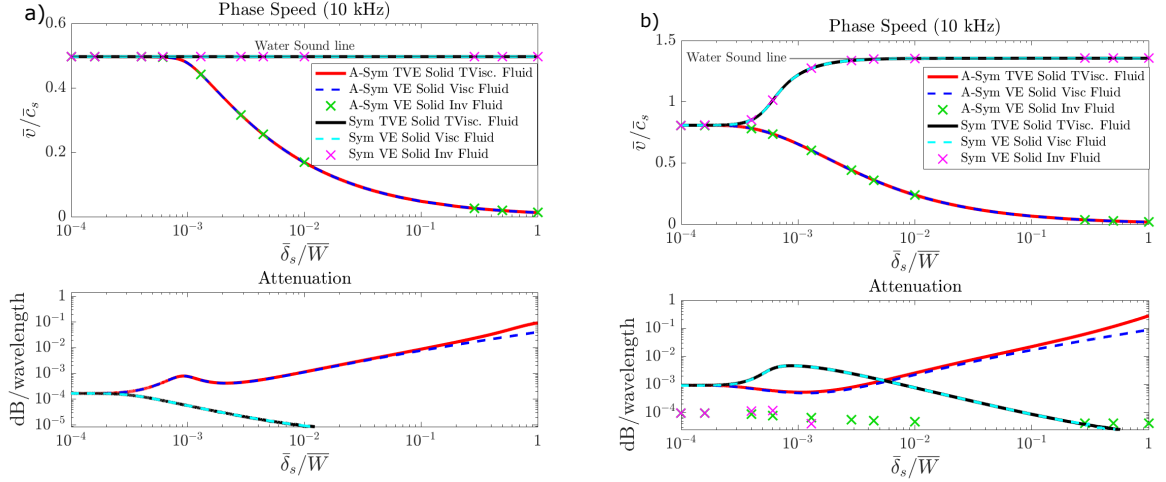


Figure 12: Relative phase speed/attenuation at 10 kHz for coupled Sc modes in water-loaded solid dissipative plates of decreasing width for: a) Steel, and b) PVC, whose material properties are in Tables 1, 2. The initial values (thick plate limit) are dictated by the Stoneley DE (3.4) and therefore the initial phase speeds are equivalent to those in Figure 6 (noting the change in non-dimensionalisation).

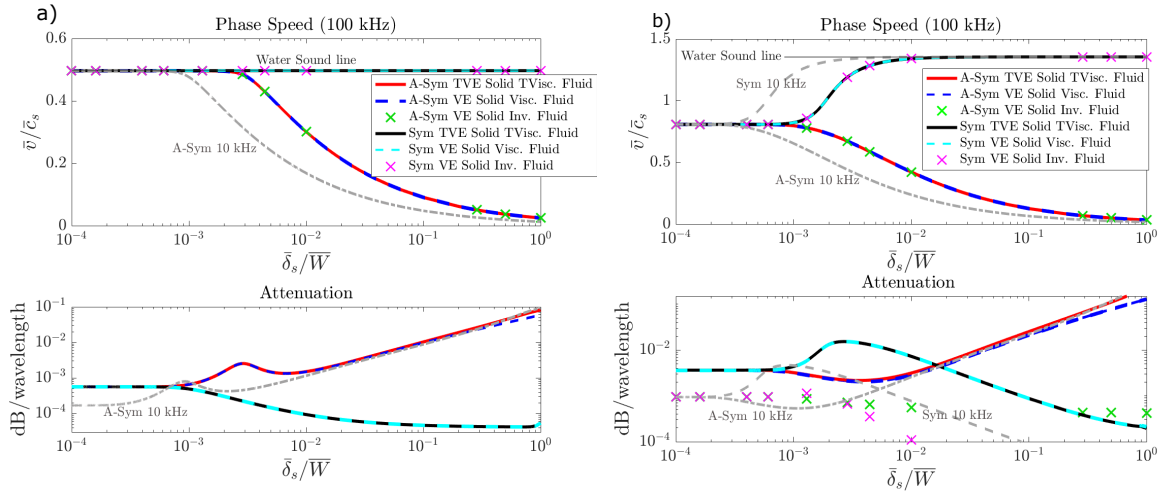


Figure 13: Relative phase speed/attenuation at 100 kHz for coupled Sc modes in water-loaded solid dissipative solid plates of decreasing width for: a) Steel, and b) PVC, whose material properties are in Tables 1, 2. The curves in grey correspond to the TVE Sym/A-Sym Coupled Sc mode for viscous water at 10 kHz, represented as black and red curves in Figure 12. Except for the phase speed of the Sym mode in a), notable dispersive effects in phase speed and attenuation are observable in both media.

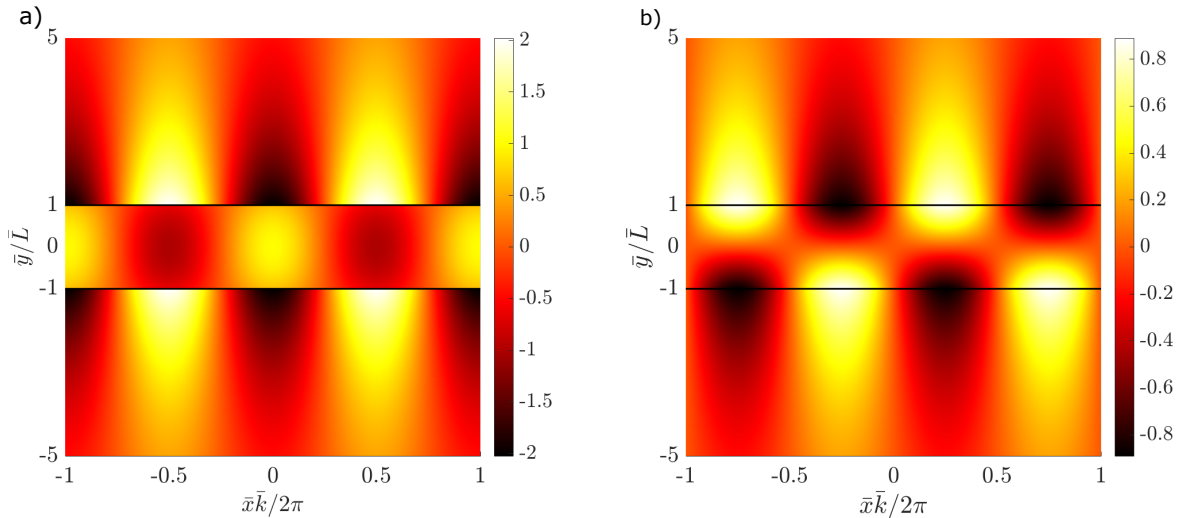


Figure 14: Real part of the displacement fields for the symmetric coupled Sc mode propagating in a PVC plate immersed in water at 10 kHz, for a plate thickness of  $\bar{\delta}_s/\bar{W} = 10^{-3}$  with values from Table 1 and DE (4.2). a) represents the horizontal particle displacement  $\text{Re}\{u_x(x, y)\}$ , and b) the vertical displacement  $\text{Re}\{u_y(x, y)\}$ . The plots have been normalized such that  $u_x(y = x = 0) = 1$ , and different lengthscales are used for the  $x$  and  $y$  directions, with the black lines representing the plate boundaries. The difference in the values of the colorbar show that the predominant motion is parallel to the interface.

(Fig 15a).

In Figure 16 we give direct comparisons of (the absolute value of) the particle displacements as seen in Figs 14, 15 for  $y \geq 0$  evaluated at  $x = 0$ , as well as the equivalent results for a steel water-loaded plate (all curves are solutions to the VE DEs (4.2), (4.4)). From Fig 16a) we first observe how indeed for the symmetric mode the parallel particle displacement  $u_x$  is dominant over the perpendicular  $u_y$ . For PVC we observe a decay within the fluid region, as opposed to water–steel, where the majority of the motion (hence energy) lies in the fluid region, with no decay observed. This situation resembles the half-space observations e.g. Figure 3d), where we essentially have compressional waves at grazing incidence in the fluid region travelling at the sound speed (Fig 12a)), with little coupling in the plate region. For the anti-symmetric mode (Fig 16b) in water–PVC, we note the more rapid decay of the motion within the fluid, whereas for water–steel we again observe a significantly larger magnitude of the horizontal particle displacement in the fluid region, although here the decay is noticed, in agreement with [25]. Note that the apparent discontinuities for  $u_x$  at the plate interface  $\bar{y} = \bar{L}$  are simply due to the extremely thin boundary layer regions (as in Fig 8a)) with the chosen parameters ( $\bar{\delta}_s/\bar{W} = 10^{-3}$  at 10 kHz) which make them not visible at the provided  $y$  scale.

#### 4.4.3 Influence of stress relaxation

Finally, we want to pay attention to the effect of stress relaxation on the soft plate and observe the corresponding effects on the phase speed/attenuation of the coupled Scholte mode. As we have done in Sections 3.3.3, 4.3.3 we proceed by letting the Young’s modulus of the plate  $E_1(\omega)$

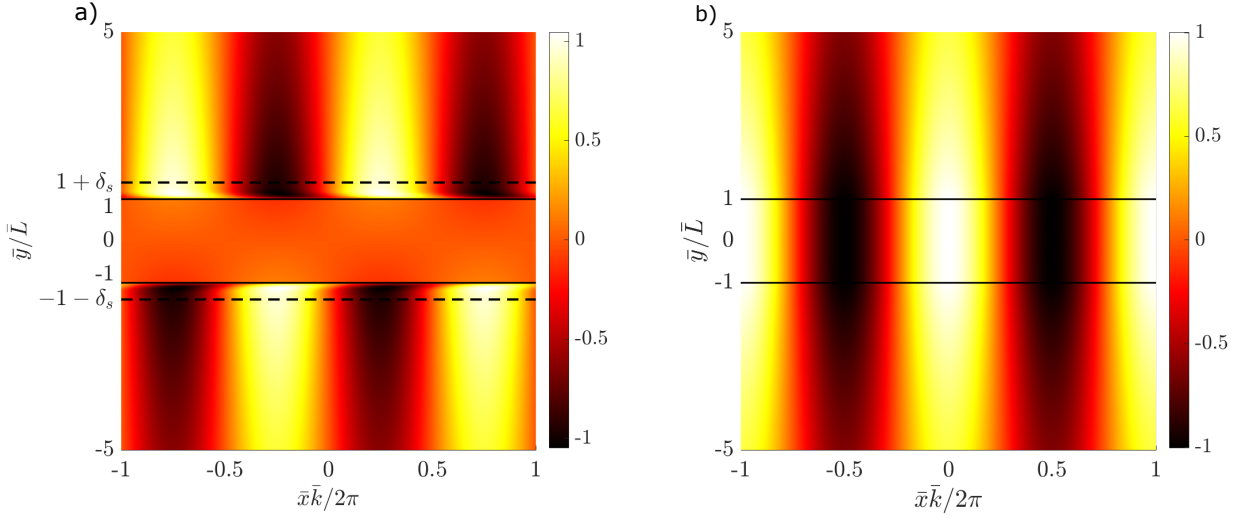


Figure 15: Real part of the displacement fields for the anti-symmetric coupled Sc mode propagating in a PVC plate immersed in water at 10 kHz, for a plate thickness of  $\bar{\delta}_s/\bar{W} = 0.2$  with values from Table 1 and DE (4.4). a) represents the horizontal particle displacement  $\text{Re}\{u_x(x, y)\}$ , and b) the vertical displacement  $\text{Re}\{u_y(x, y)\}$ . The plots have been normalized such that  $u_y(y = x = 0) = 1$ , and different lengthscales are used for the  $x$  and  $y$  directions with the black lines representing the plate boundaries.

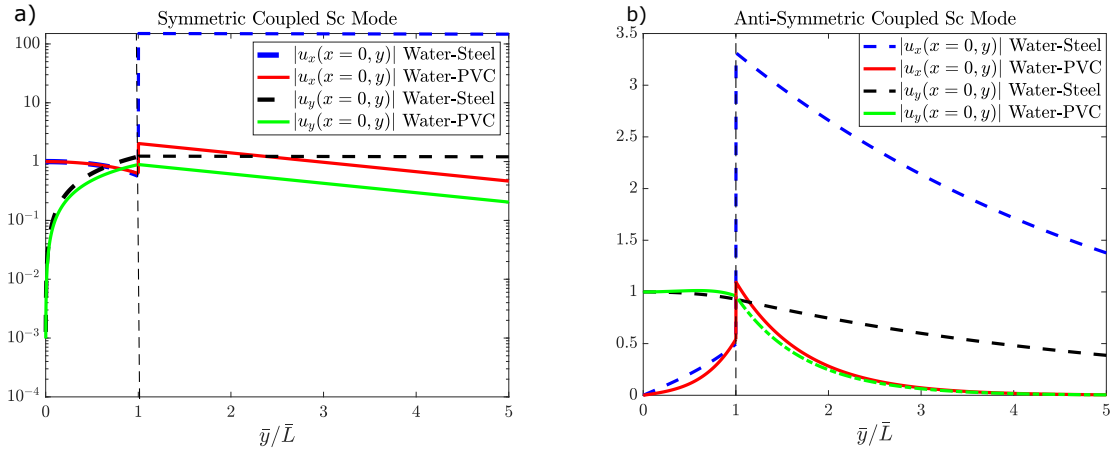


Figure 16: Comparisons between the magnitude of the components of the displacement fields of steel/PVC plates loaded with water at 10 kHz for the sym. coupled Sc mode (a), and the anti-sym. coupled Sc mode (b) normalized in each case s.t. the displacement at the center of the plate is 1. The plate thickness is  $\bar{\delta}_s/\bar{W} = 10^{-3}$  with values from Table 1. The apparent discontinuities for  $u_x$  at the plate interface  $y = 1$  are simply due to the thinness of the boundary layer region with the large  $y$  scale employed.

follow the SLSM whilst its Poisson's ratio  $\nu_1$  remains constant, as in (3.10) (with subscripts in the moduli interchanged from '2' to '1') noting that  $t_r = \bar{c}_s \bar{t}_r / \bar{L}$ . In the illustrations below we also let  $\bar{E}_\infty = 4.4524$  GPa so that the rubbery phase limit of the PVC material corresponds to the (fixed) value from Table 1 (as we did for the slits in Section 4.3.3) and ignore thermal effects.

In Figure 17 we give the phase speed/attenuation of the symmetric and anti-symmetric coupled Sc mode as a function of plate thickness (as in Fig 12) with fixed Deborah numbers  $\omega t_r = 0.1, 1, 50$  so that we cover the rubbery and glassy phases, as well as glass transition. Furthermore, in this figure we have chosen a moderate value of the ratio  $\bar{E}_0 / \bar{E}_\infty = 1.58$ , see Figure 4b). For the anti-symmetric mode (Figure 17a)) we observe how the initial phase speed values dictated by the Stoneley DE (3.4) become higher when the material is in the glassy phase, which then tend to zero in the thin plate limit following the observations in Figure 12. In terms of attenuation, we first observe the remarkably higher values for  $\omega t_r = 0.1, 1$  (at all plate widths) when compared to the KVM results from Figure 12. For the anti-symmetric mode (Figure 17a)) we observe that the attenuation (per wavelength) approaches non-zero values (except for  $\omega t_r \gg 1$ ) in the thin plate limit. With regards to the symmetric mode (Figure 17b)) we first note that the initial behaviour in both phase speed and attenuation is identical to that of the anti-symmetric mode, as expected following our discussion above. As the plate width decreases, the mode first enters the dispersive region and continues to asymptote towards the fluid's phase speed  $\bar{v} / \bar{c}_s = 1.35$  following the observations from Figure 12. When it comes to the attenuation, the global maximum discussed above become significantly enhanced in the dispersive region (particularly for  $\omega t_r \approx 1$ ), after which it monotonically decreases towards zero as the root approaches the fluid's (constant) bulk mode.

It is worth stressing that this global maximum for the symmetric coupled Sc only arises when the mode's phase speed is dispersive which (for a fixed fluid) requires soft media, so that  $\rho_s \approx 1$ . For this reason we did not observe it for water-loaded steel plates in Figure 12a), noting that is the main focus of existing literature [3]. Some further tests (not shown) confirmed that the inclusion of fluid viscosity has little influence on the presence of this maximum, so that solutions to (4.6a) (corresponding to  $\eta_{\mu_2} = 0$ ) accurately capture this global maximum (as expected given the little magnitude of boundary layer attenuation in Figure 12). This can also be noticed by the VE Solid–Inviscid fluid results (pink crosses) in the bottom of Fig 13b), albeit smaller due to the absence of fluid viscosity, the local maximum can still be appreciated.

Perhaps surprisingly, we have not been able to find discussions about this feature in the existing literature.

## 5 Conclusions

This paper has focused on the influence of thermo-viscous damping in some of the principal modes of wave propagation in two physical systems, namely fluid-filled slits embedded in infinitely extending solids, and fluid-loaded plates, where the fluid considered is water. These two settings are connected by the fact that the respective waves in the short wavelength limit (with respect to channel/plate width) are governed by the same dispersion equation, namely the Scholte-Stoneley DE. The direct correspondence between the governing equations for thermo-visco-acoustic fluids and thermo-visco-elasticity developed in [1] is used in order to obtain generalised dispersion relations for symmetric and anti-symmetric modes that can govern the two specific set-ups of interest when taking the appropriate limits, which is a particularly convenient aspect of this study.

For fluid-filled channels, the results are presented as an extension of earlier work by some of the present authors [2]. We firstly show how the consideration of soft media requires paying more attention to the way the roots are initially found, as a result of the Scholte mode's phase speed

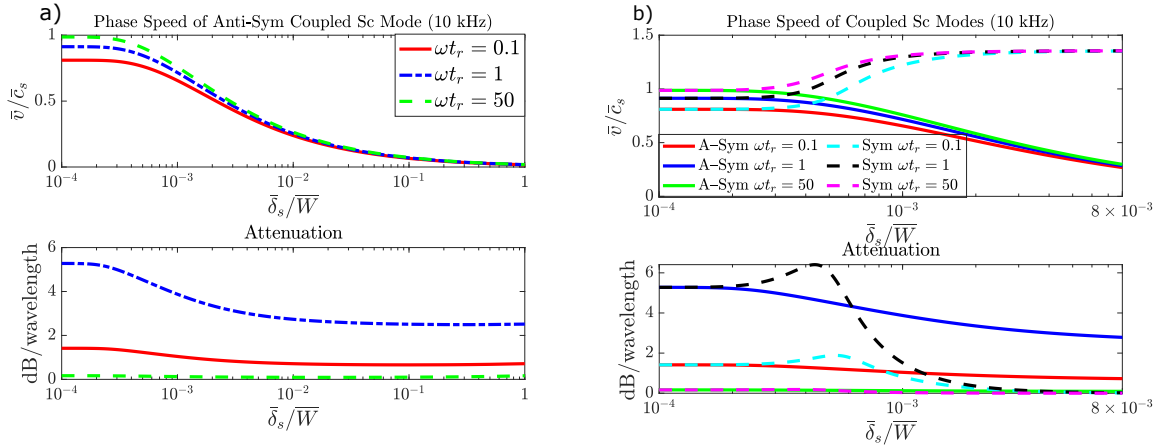


Figure 17: Relative phase speed/attenuation at 10 kHz for coupled Sc modes in water-loaded VE PVC plates of decreasing width according to the SLSM with  $\bar{E}_0/\bar{E}_\infty = 1.58$ , whilst keeping the Deborah number fixed (and in all cases  $\bar{c}_s = 1100$  m/s). The fluid is assumed to be viscous so that all the curves correspond to roots of (4.2) and (4.4). In a) we only show the anti-symmetric mode for a very wide range of plate widths, whereas in b) we also include the symmetric mode for plate thicknesses in the region of interest. In particular, we note the enhancement of the global attenuation maxima for the symmetric mode which subsequently tends to zero as the mode becomes non-dispersive.

reduction (from the fluid sound line) in water-(soft) solid interfaces. We then emphasise how viscoelastic mechanisms in the solid affect the overall attenuation at different frequency ranges and channel widths, for both the commonly used Kelvin-Voigt model (KVM) and the standard linear solid model (SLSM), which incorporates stress relaxation. It has been shown how stress relaxation can greatly affect the phase speed and attenuation of the mode, and in particular the ability to damp energy if the mode can be excited around the glass transition of the material which is characterized by a Deborah number of one, i.e.  $\omega t_r = 1$ . As a result of including thermal coupling, we are also able to justify the claim made in [2] that for water-filled slits, thermal effects do not add any significant changes in the regions considered.

For fluid-loaded plates, the work here builds on the work in [3]. Utilizing the same root finding technique as for the channels, where the initial value is based on the Scholte-Stoneley DE behaviour, the dispersion of the phase speed of both the symmetric and anti-symmetric modes as a function of plate thickness is analysed, as well the associated displacement fields. We originally observe very little dissipation compared to the slit case as a result of the boundary layers being localized on the exterior sides of the plate and therefore never interacting regardless of the thinness of the plate. Nevertheless, the presence of a global maximum in the attenuation of the symmetric coupled Scholte mode is noticed for the soft solid only, indicating that it is closely linked to the dispersion in phase speed, and therefore not observed for hard water-solid interfaces. The attenuation increases significantly for both modes when stress relaxation is included in the soft plate, and in the thin-plate limit the attenuation of anti-symmetric modes tends to constant non-zero values for each  $\omega t_r$ , whereas the dissipation of the symmetric mode becomes zero as soon as the phase speed becomes constant. Nevertheless, the global maximum in attenuation observed previously is largely enhanced, particularly around glass transition. We believe that this global maximum should be observable

experimentally following the work in [3] and perhaps can even be interesting to the non-destructive evaluation/testing community for possible applications.

More generally and perhaps critically, we find that although the widely used KVM (even with varying viscosity coefficient to match experimental results) can accurately predict the loss at particular frequencies as shown in e.g. [15], with such models the dispersion of the real parts of these elastic moduli (and hence phase speed of the associated modes) cannot be captured. We show this can be crucially important, particularly at frequencies near the glass transition. We further note that the SLSM used here to capture stress relaxation, namely Prony series with a single relaxation time, is the simplest model that captures long time solid-like ‘glassy’ behaviour and generally, the VE behaviour of polymers is much more complex [43, 18]. Furthermore, the relaxation results are based around a PVC sample with  $\bar{E}_\infty = 4.4524$  GPa, such that the half-space Scholte mode propagates at a phase speed approximately 60% of that of water and is therefore considered soft in this context, especially when compared to the steel sample analysed here, for which the Scholte mode propagates essentially at the speed of sound of water. Nevertheless, the amplitude ratio  $\bar{E}_0/\bar{E}_\infty$  is well known to become particularly large for significantly softer media, although in terms of practicality this is offset by the fact that in this regime the Scholte mode is likely to be much more difficult to excite. These results strongly motivate the need for further experimental results in the frequencies of interest in order to be able to ascertain under which conditions these mechanisms can be exploited, as well as relevant data for relaxation times and short/long time moduli.

## REFERENCES

- [1] Erik García Neeffjes, David Nigro, Artur L Gower, Raphaël C Assier, Valerie J Pinfield, and William J Parnell. A unified framework for linear thermo-visco-elastic wave propagation including the effects of stress-relaxation. *Proceedings of the Royal Society A*, 478(2265):20220193, 2022.
- [2] PA Cotterill, D Nigro, ID Abrahams, E Garcia-Neeffjes, and WJ Parnell. Thermo-viscous damping of acoustic waves in narrow channels: A comparison of effects in air and water. *The Journal of the Acoustical Society of America*, 144(6):3421–3436, 2018.
- [3] BM Staples, TJ Graham, AP Hibbins, and JR Sambles. Coupled Scholte modes supported by soft elastic plates in water. *Physical Review E*, 103(6):063002, 2021.
- [4] Joseph L Rose. *ultrasonic guided waves in solid media*. Cambridge University Press, 2014.
- [5] Sjoerd W Rienstra. Fundamentals of duct acoustics. *Von Karman Institute Lecture Notes*, 2015.
- [6] GP Ward, RK Lovelock, ARJ Murray, AP Hibbins, JR Sambles, and JD Smith. Boundary-layer effects on acoustic transmission through narrow slit cavities. *Physical review letters*, 115(4):044302, 2015.
- [7] G Kirchhoff. Ueber den einfluss der wärmeleitung in einem gase auf die schallbewegung. *Annalen der Physik*, 210(6):177–193, 1868.
- [8] M Bruneau. *Fundamentals of acoustics*. John Wiley & Sons, 2013.
- [9] Q Qi. Attenuated leaky Rayleigh waves. *The Journal of the Acoustical Society of America*, 95(6):3222–3231, 1994.

- [10] VA Gusev and PA Simonova. Effect of shear components of the acoustic field in the viscous liquid on the structure of the Stoneley wave at the interface between the liquid and elastic half-spaces. *Physics of Wave Phenomena*, 23(4):268–272, 2015.
- [11] J Zhu, JS Popovics, and F Schubert. Leaky Rayleigh and Scholte waves at the fluid–solid interface subjected to transient point loading. *The Journal of the Acoustical Society of America*, 116(4):2101–2110, 2004.
- [12] N Favretto-Anrès. Theoretical study of the Stoneley-Scholte wave at the interface between an ideal fluid and a viscoelastic solid. *Acta Acustica united with Acustica*, 82(6):829–838, 1996.
- [13] C Glorieux, K Van de Rostyne, K Nelson, W Gao, W Lauriks, and J Thoen. On the character of acoustic waves at the interface between hard and soft solids and liquids. *The Journal of the Acoustical Society of America*, 110(3):1299–1306, 2001.
- [14] VG Mozhaev and M Weihnacht. Subsonic leaky Rayleigh waves at liquid–solid interfaces. *Ultrasonics*, 40(1-8):927–933, 2002.
- [15] N Favretto-Anrès and G Rabau. Excitation of the Stoneley–Scholte wave at the boundary between an ideal fluid and a viscoelastic solid. *Journal of sound and vibration*, 203(2):193–208, 1997.
- [16] N Favretto-Anres and JP Sessarego. Identification of shear wave parameters of viscoelastic solids by laboratory measurements of Stoneley-Scholte waves. *Acta Acustica United with Acustica*, 85(4):505–516, 1999.
- [17] M Zajac, H Kahl, B Schade, T Rödel, M Dionisio, and M Beiner. Relaxation behavior of polyurethane networks with different composition and crosslinking density. *Polymer*, 111:83–90, 2017.
- [18] Y Liao and V Wells. Estimation of complex modulus using wave coefficients. *Journal of Sound and Vibration*, 295(1-2):165–193, 2006.
- [19] CY Hui and A Jagota. Effect of surface tension on the relaxation of a viscoelastic half-space perturbed by a point load. *Journal of Polymer Science Part B: Polymer Physics*, 54(2):274–280, 2016.
- [20] MFM Osborne and SD Hart. Transmission, reflection, and guiding of an exponential pulse by a steel plate in water. i. theory. *The Journal of the Acoustical Society of America*, 17(1):1–18, 1945.
- [21] A Schoch. Der schalldurchgang durch platten. *Acta Acustica united with Acustica*, 2(1):1–17, 1952.
- [22] Z Zhu and J Wu. The propagation of Lamb waves in a plate bordered with a viscous liquid. *The Journal of the Acoustical Society of America*, 98(2):1057–1064, 1995.
- [23] J Wu and Z Zhu. An alternative approach for solving attenuated leaky Rayleigh waves. *The Journal of the Acoustical Society of America*, 97(5):3191–3193, 1995.
- [24] AH Nayfeh and PB Nagy. Excess attenuation of leaky Lamb waves due to viscous fluid loading. *The Journal of the Acoustical Society of America*, 101(5):2649–2658, 1997.

- [25] FB Cegla, P Cawley, and MJS Lowe. Material property measurement using the quasi-Scholte mode—a waveguide sensor. *The Journal of the Acoustical Society of America*, 117(3):1098–1107, 2005.
- [26] X Xu, J Goossens, G Shkerdin, and C Glorieux. Effect of loading a plate with different liquids on the propagation of lamb-like waves studied by laser ultrasonics. *IEEE transactions on ultrasonics, ferroelectrics, and frequency control*, 55(3):675–685, 2008.
- [27] R Christensen. *Theory of viscoelasticity: an introduction*. Elsevier, 2012.
- [28] NW Tschoegl, WG Knauss, and I Emri. Poisson’s ratio in linear viscoelasticity—a critical review. *Mechanics of Time-Dependent Materials*, 6(1):3–51, 2002.
- [29] RD Borchardt. *Viscoelastic waves in layered media*. Cambridge University Press, 2009.
- [30] R Stoneley. Elastic waves at the surface of separation of two solids. *Proceedings of the Royal Society of London. Series A, Containing Papers of a Mathematical and Physical Character*, 106(738):416–428, 1924.
- [31] L Rayleigh. On waves propagated along the plane surface of an elastic solid. *Proceedings of the London mathematical Society*, 1(1):4–11, 1885.
- [32] CT Schröder and WR Scott Jr. On the complex conjugate roots of the Rayleigh equation: The leaky surface wave. *The Journal of the Acoustical Society of America*, 110(6):2867–2877, 2001.
- [33] JG Harris and JD Achenbach. Comment on “on the complex conjugate roots of the Rayleigh equation: The leaky surface wave” [j. acoust. soc. am. 110, 2867 (2001)](1). *The Journal of the Acoustical Society of America*, 112(5):1747–1748, 2002.
- [34] AD Pierce et al. *Acoustics: an introduction to its physical principles and applications*, volume 678. McGraw-Hill New York, 1981.
- [35] MM Volkenshtein and VM Levin. Structure of a Stoneley wave at an interface between a viscous-fluid and a solid. *SOVIET PHYSICS ACOUSTICS*, 34(4):351–355, 1988.
- [36] PB Nagy and AH Nayfeh. Viscosity-induced attenuation of longitudinal guided waves in fluid-loaded rods. *The Journal of the Acoustical Society of America*, 100(3):1501–1508, 1996.
- [37] SC Hunter. *Mechanics of continuous media*. Halsted Press, 1976.
- [38] N Obaid, MT Kortschot, and M Sain. Understanding the stress relaxation behavior of polymers reinforced with short elastic fibers. *Materials*, 10(5):472, 2017.
- [39] T Chen. Determining a prony series for a viscoelastic material from time varying strain data, 21p. NASA, 2000.
- [40] WJ Parnell and R De Pascalis. Soft metamaterials with dynamic viscoelastic functionality tuned by pre-deformation. *Philosophical Transactions of the Royal Society A*, 377(2144):20180072, 2019.
- [41] SI Rokhlin, DE Chimenti, and AH Nayfeh. On the topology of the complex wave spectrum in a fluid-coupled elastic layer. *The Journal of the Acoustical Society of America*, 85(3):1074–1080, 1989.

- [42] X Jia. Modal analysis of Lamb wave generation in elastic plates by liquid wedge transducers. *The Journal of the Acoustical Society of America*, 101(2):834–842, 1997.
- [43] WN Sharpe. *Springer handbook of experimental solid mechanics*. Springer Science & Business Media, 2008.
- [44] Witold Nowacki. *Thermoelasticity*. Elsevier, 2013.
- [45] VA Lubarda. On thermodynamic potentials in linear thermoelasticity. *International Journal of Solids and Structures*, 41(26):7377–7398, 2004.

# Appendices

## A Inclusion of thermal expansion effects

Despite a priori not expecting to add major differences to the physical results obtained with the VE theory presented in the main text since water is the only fluid media used in the calculations, we discuss how to obtain the more general thermo-visco-elastic (TVE) equivalent equations from the governing equations.

Thermal Parameters						
Parameter	Unit	Symbol	Water	Steel	PVC	$M_{\tau=0.9}$
Ratio of specific heats	–	$\gamma$	1.0095	1.0034	1.05	1.048
Specific heat at constant volume	[J kg <sup>-1</sup> K <sup>-1</sup> ]	$c_v$	4188	498.325	1238.09	1164.11
Ambient temperature	[K]	$T_0$	283.16	293	300	299.3
Thermal conductivity	[W m <sup>-1</sup> K <sup>-1</sup> ]	$\mathcal{K}$	0.597	30	2	4.8
Coefficient of thermal expansion	[K <sup>-1</sup> ]	$\alpha$	$8.16 \times 10^{-5}$	$1.7 \times 10^{-5}$	$3.5 \times 10^{-4}$	$2.2 \times 10^{-4}$

Table 2: Thermal parameter values used for water, steel and PVC employed in the TVE calculations throughout. Recall that  $M_{\tau=0.9}$  is a made-up material defined in (3.9).

### A.1 Governing equations

Following [1] we have that, when taking into account strain histories but ignoring corresponding thermal histories, a Helmholtz free energy can be derived (from a state of zero strain  $\hat{\boldsymbol{\varepsilon}} = \mathbf{0}$  and constant temperature  $T = T_0$ ) from which the stress strain relations and entropy follow, namely

$$\hat{\boldsymbol{\sigma}} = \int_{-\infty}^t 2\hat{\mu}(t - \mathcal{T}) \frac{\partial \hat{\boldsymbol{\varepsilon}}(\mathcal{T})}{\partial \mathcal{T}} d\mathcal{T} + \left( \int_{-\infty}^t \hat{K}(t - \mathcal{T}) \text{tr} \left( \frac{\partial \hat{\boldsymbol{\varepsilon}}(\mathcal{T})}{\partial \mathcal{T}} \right) d\mathcal{T} - \alpha T_0 K \hat{\theta} \right) \mathbf{I}, \quad (\text{A.1a})$$

$$\hat{\mathbf{s}} = \mathbf{s}_0 + c_v \hat{\theta} + \frac{\alpha K}{\rho_0} \text{tr}(\hat{\boldsymbol{\varepsilon}}), \quad (\text{A.1b})$$

where  $T_0$ ,  $\hat{\theta} = (T - T_0)/T_0$  represent the background temperature and non-dimensional temperature,  $\alpha$  is the coefficient of thermal expansion,  $\hat{\mathbf{s}}$  denotes the entropy per unit mass and  $c_v$  is the specific heat at constant volume (strain) which is related to the specific heat at constant pressure (stress)  $c_p$  by  $c_p/c_v = \gamma$  where  $\gamma$  denotes the ratio of specific heats. Naturally, we must still satisfy the

momentum equations (2.1) together with the energy balance equation, which is given by

$$\mathcal{K} \Delta \hat{\theta} - \rho_0 c_v \frac{\partial \hat{\theta}}{\partial t} = \alpha K \operatorname{tr} \left( \frac{\partial \hat{\boldsymbol{\varepsilon}}(\mathcal{T})}{\partial \mathcal{T}} \right), \quad (\text{A.2})$$

where  $\mathcal{K}$  is the thermal conductivity (the units of these newly introduced thermal quantities are summarized in Table 2). Assuming now that the fields are time-harmonic, of the form

$$\{\hat{\mathbf{u}}, \hat{\theta}, \hat{\boldsymbol{\sigma}}, \hat{\boldsymbol{\varepsilon}}, \hat{\mathbf{e}}\}(\mathbf{x}, t) = \operatorname{Re} \{ \{ \mathbf{u}, \theta, \boldsymbol{\sigma}, \boldsymbol{\varepsilon}, \mathbf{e} \}(\mathbf{x}) e^{-i\omega t} \}, \quad (\text{A.3})$$

we show in detail in [1] that introducing the wave potentials in the Helmholtz form

$$\mathbf{u} = \nabla(\varphi + \vartheta) + \nabla \times \boldsymbol{\Phi}, \quad \nabla \cdot \boldsymbol{\Phi} = 0, \quad (\text{A.4})$$

the governing equations (2.1), (A.2) reduce to solving

$$\Delta \vartheta + k_\vartheta^2 \vartheta = 0, \quad \Delta \varphi + k_\varphi^2 \varphi = 0, \quad \Delta \boldsymbol{\Phi} + k_\Phi^2 \boldsymbol{\Phi} = \mathbf{0}, \quad (\text{A.5})$$

where the thermo-compressional wavenumbers can be written as

$$k_\vartheta^2 = a + b, \quad k_\varphi^2 = a - b, \quad a = \frac{1}{2} (k_\theta^2 + k_\phi^2 - L_\theta L_\phi), \quad \text{and} \quad b = \sqrt{a^2 - k_\phi^2 k_\theta^2}, \quad (\text{A.6})$$

and

$$k_\theta^2 = i c_v \frac{\rho_0 \omega}{\mathcal{K}}, \quad k_\phi^2 = \frac{\rho_0 \omega^2}{\hat{K}(\omega) + \frac{4}{3} \hat{\mu}(\omega)}, \quad k_\Phi^2 = \frac{\rho_0 \omega^2}{\hat{\mu}(\omega)}, \quad L_\phi = \frac{i \alpha K \omega}{\mathcal{K}}, \quad L_\theta = -\frac{\alpha T_0 K}{\hat{\lambda}(\omega) + 2 \hat{\mu}(\omega)}. \quad (\text{A.7})$$

Furthermore, the corresponding temperature difference field is given by  $\theta = \mathcal{T}_\varphi \varphi + \mathcal{T}_\vartheta \vartheta$ , where  $\mathcal{T}_\varphi = (k_\varphi^2 - k_\phi^2)/L_\theta$  and similarly  $\mathcal{T}_\vartheta = (k_\vartheta^2 - k_\phi^2)/L_\theta$ .

## A.2 The TVE Stoneley-Scholte Dispersion Equation

Given the generalised equations in the TVE context presented above (A.4), (A.5) the potentials in (3.1) are now written as

$$\bar{\varphi}_1 = \bar{P}_1 e^{-\bar{\gamma}_{\varphi_1} \bar{y} + i \bar{k} \bar{x}}, \quad \bar{\varphi}_2 = \bar{P}_2 e^{\bar{\gamma}_{\varphi_2} \bar{y} + i \bar{k} \bar{x}}, \quad (\text{A.8a})$$

$$\bar{\vartheta}_1 = \bar{T}_1 e^{-\bar{\gamma}_{\vartheta_1} \bar{y} + i \bar{k} \bar{x}}, \quad \bar{\vartheta}_2 = \bar{T}_2 e^{\bar{\gamma}_{\vartheta_2} \bar{y} + i \bar{k} \bar{x}}, \quad (\text{A.8b})$$

$$\bar{\boldsymbol{\Phi}}_1 = \bar{S}_1 e^{-\bar{\gamma}_{\Phi_1} \bar{y} + i \bar{k} \bar{x}}, \quad \bar{\boldsymbol{\Phi}}_2 = \bar{S}_2 e^{\bar{\gamma}_{\Phi_2} \bar{y} + i \bar{k} \bar{x}}, \quad (\text{A.8c})$$

where  $\bar{\gamma}_{\Phi_1}, \bar{\gamma}_{\Phi_2}$  remain identical to those in the isothermal case (3.2) whereas

$$\bar{\gamma}_{\varphi_1} = (\bar{k}^2 - \bar{k}_{\varphi_1}^2)^{1/2}, \quad \bar{\gamma}_{\varphi_2} = (\bar{k}^2 - \bar{k}_{\varphi_2}^2)^{1/2}, \quad \bar{\gamma}_{\vartheta_1} = (\bar{k}^2 - \bar{k}_{\vartheta_1}^2)^{1/2}, \quad \bar{\gamma}_{\vartheta_2} = (\bar{k}^2 - \bar{k}_{\vartheta_2}^2)^{1/2}, \quad (\text{A.9})$$

for some complex amplitudes  $\bar{P}_1, \bar{P}_2, \bar{T}_1, \bar{T}_2, \bar{S}_1, \bar{S}_2$ . As discussed above, we must ensure that the choice of the various branch cuts of the square root functions in (A.9) is consistent with causality. At the interface between the two media, the solutions must again satisfy continuity of traction and displacement, and in addition, continuity of temperature and temperature flux BCs, that is on  $\bar{y} = 0$ ,

$$\bar{\sigma}_{yy}^1 = \bar{\sigma}_{yy}^2, \quad \bar{\sigma}_{xy}^1 = \bar{\sigma}_{xy}^2, \quad \bar{\mathbf{u}}_1 = \bar{\mathbf{u}}_2, \quad \theta_1 = \theta_2, \quad \bar{\mathcal{K}}_1 \bar{\nabla} \theta_1 \cdot \mathbf{e}_y = \bar{\mathcal{K}}_2 \bar{\nabla} \theta_2 \cdot \mathbf{e}_y. \quad (\text{A.10})$$

Substitution of (A.8) into (A.10) then yields a homogenous linear system, whose non-trivial solutions are given by

$$\det \bar{\mathbf{A}} = 0, \quad (\text{A.11})$$

where

$$\bar{\mathbf{A}} = \begin{pmatrix} 2\bar{k}^2\bar{\mu}_1 - \bar{\alpha}_1\bar{T}_1\bar{K}_1\bar{\mathcal{T}}_{\varphi_1} - \bar{k}_{\varphi_1}^2\bar{\Gamma}_1 & -2i\bar{\gamma}_{\varphi_1}\bar{k}\bar{\mu}_1 & -2i\bar{\gamma}_{\vartheta_1}\bar{k}\bar{\mu}_1 & \bar{\mu}_1(2\bar{k}^2 - \bar{k}_{\Phi_1}^2) \\ i\bar{k} & i\bar{k} & i\bar{k} & 2i\bar{\gamma}_{\Phi_1}\bar{k}\bar{\mu}_1 \\ -\bar{\gamma}_{\varphi_1} & -\bar{\gamma}_{\vartheta_1} & -\bar{\gamma}_{\vartheta_1} & -\bar{\gamma}_{\Phi_1} \\ \bar{\mathcal{T}}_{\varphi_1} & \bar{\mathcal{T}}_{\vartheta_1} & \bar{\mathcal{T}}_{\vartheta_1} & -i\bar{k} \\ \bar{\gamma}_{\varphi_1}\bar{\mathcal{K}}_1\bar{\mathcal{T}}_{\varphi_1} & \bar{\gamma}_{\vartheta_1}\bar{\mathcal{K}}_1\bar{\mathcal{T}}_{\vartheta_1} & \bar{\gamma}_{\vartheta_1}\bar{\mathcal{K}}_1\bar{\mathcal{T}}_{\vartheta_1} & 0 \\ -2\bar{k}^2\bar{\mu}_2 + \bar{\alpha}_2\bar{T}_2\bar{K}_2\bar{\mathcal{T}}_{\varphi_2} + \bar{k}_{\varphi_2}^2\bar{\Gamma}_2 & -2i\bar{\gamma}_{\varphi_2}\bar{k}\bar{\mu}_2 & -2i\bar{\gamma}_{\vartheta_2}\bar{k}\bar{\mu}_2 & -\bar{\mu}_2(2\bar{k}^2 - \bar{k}_{\Phi_2}^2) \\ -i\bar{k} & -i\bar{k} & -i\bar{k} & 2i\bar{\gamma}_{\Phi_2}\bar{k}\bar{\mu}_2 \\ -\bar{\gamma}_{\varphi_2} & -\bar{\gamma}_{\vartheta_2} & -\bar{\gamma}_{\vartheta_2} & -\bar{\gamma}_{\Phi_2} \\ -\bar{\mathcal{T}}_{\varphi_2} & -\bar{\mathcal{T}}_{\vartheta_2} & -\bar{\mathcal{T}}_{\vartheta_2} & i\bar{k} \\ \bar{\gamma}_{\varphi_2}\bar{\mathcal{K}}_2\bar{\mathcal{T}}_{\varphi_2} & \bar{\gamma}_{\vartheta_2}\bar{\mathcal{K}}_2\bar{\mathcal{T}}_{\vartheta_2} & \bar{\gamma}_{\vartheta_2}\bar{\mathcal{K}}_2\bar{\mathcal{T}}_{\vartheta_2} & 0 \end{pmatrix}, \quad (\text{A.12})$$

where  $\bar{\Gamma}_i = \bar{\Gamma}_i(\omega) = \hat{K}_i(\bar{\omega}) + 4\hat{\mu}_i(\bar{\omega})/3$  for  $i = 1, 2$ . In the limit  $\bar{\alpha}_1, \bar{\alpha}_2 \rightarrow 0$  the thermal and mechanical effects fully decouple and equation (A.11) reduces to (3.4) after relabeling.

### A.3 The TVE Slit-Plate Dispersion Equations

For symmetric modes, the generalisation to (4.1) in this setting is given by

$$\bar{\varphi}_1 = \bar{P}1_S \cosh(\bar{\gamma}_{\varphi_1}\bar{y})e^{i\bar{k}\bar{x}}, \quad \bar{\varphi}_2(\bar{x}, \bar{y}) = \begin{cases} \bar{P}2_S e^{\bar{\gamma}_{\varphi_2}(\bar{y}+\bar{L})+i\bar{k}\bar{x}}, & \bar{y} \leq -\bar{L} \\ \bar{P}2_S e^{-\bar{\gamma}_{\varphi_2}(\bar{y}-\bar{L})+i\bar{k}\bar{x}}, & \bar{y} \geq \bar{L} \end{cases}, \quad (\text{A.13a})$$

$$\bar{\vartheta}_1 = \bar{T}1_S \cosh(\bar{\gamma}_{\vartheta_1}\bar{y})e^{i\bar{k}\bar{x}}, \quad \bar{\vartheta}_2(\bar{x}, \bar{y}) = \begin{cases} \bar{T}2_S e^{\bar{\gamma}_{\vartheta_2}(\bar{y}+\bar{L})+i\bar{k}\bar{x}}, & \bar{y} \leq -\bar{L} \\ \bar{T}2_S e^{-\bar{\gamma}_{\vartheta_2}(\bar{y}-\bar{L})+i\bar{k}\bar{x}}, & \bar{y} \geq \bar{L} \end{cases}, \quad (\text{A.13b})$$

$$\bar{\Phi}_1 = \bar{S}1_S \sinh(\bar{\gamma}_{\Phi_1}\bar{y})e^{i\bar{k}\bar{x}}, \quad \bar{\Phi}_2(\bar{x}, \bar{y}) = \begin{cases} \bar{S}2_S e^{\bar{\gamma}_{\Phi_2}(\bar{y}+\bar{L})+i\bar{k}\bar{x}}, & \bar{y} \leq -\bar{L} \\ \bar{S}2_S e^{-\bar{\gamma}_{\Phi_2}(\bar{y}-\bar{L})+i\bar{k}\bar{x}}, & \bar{y} \geq \bar{L} \end{cases}, \quad (\text{A.13c})$$

for some complex valued amplitudes  $\bar{P}1_S, \bar{P}2_S, \bar{T}1_S, \bar{T}2_S, \bar{S}1_S, \bar{S}2_S$ . In this case, the continuity conditions (A.10) must be satisfied at the two interfaces between the two media  $\bar{y} = \pm\bar{L}$ . Substitution of (A.13) into (A.10) then yields an equation of the form  $\det \bar{\mathbf{A}}_{Sym} = 0$ , where  $\bar{\mathbf{A}}_{Sym}$  is given by

$$\left( \begin{array}{ccc}
2i\bar{\gamma}_{\varphi_1}\bar{k}\bar{\mu}_1 \sinh(\bar{\gamma}_{\varphi_1}\bar{L}) & 2i\bar{\gamma}_{\vartheta_1}\bar{k}\bar{\mu}_1 \sinh(\bar{\gamma}_{\vartheta_1}\bar{L}) & \bar{\mu}_1(2\bar{k}^2 - \bar{k}_{\Phi_1}^2) \sinh(\bar{\gamma}_{\Phi_1}\bar{L}) \\
\cosh(\bar{\gamma}_{\varphi_1}\bar{L})[2\bar{k}^2\bar{\mu}_1 - \bar{\alpha}_1\bar{T}_1\bar{K}_1\bar{\mathcal{T}}_{\varphi_1} - \bar{k}_{\varphi_1}^2\bar{\Gamma}_1] & \cosh(\bar{\gamma}_{\vartheta_1}\bar{L})[2\bar{k}^2\bar{\mu}_1 - \bar{\alpha}_1\bar{T}_1\bar{K}_1\bar{\mathcal{T}}_{\vartheta_1} - \bar{k}_{\vartheta_1}^2\bar{\Gamma}_1] & -2i\bar{\gamma}_{\Phi_1}\bar{k}\bar{\mu}_1 \cosh(\bar{\gamma}_{\Phi_1}\bar{L}) \\
i\bar{k} \cosh(\bar{\gamma}_{\varphi_1}\bar{L}) & i\bar{k} \cosh(\bar{\gamma}_{\vartheta_1}\bar{L}) & \bar{\gamma}_{\Phi_1} \cosh(\bar{\gamma}_{\Phi_1}\bar{L}) \\
\bar{\gamma}_{\varphi_1} \sinh(\bar{\gamma}_{\varphi_1}\bar{L}) & \bar{\gamma}_{\vartheta_1} \sinh(\bar{\gamma}_{\vartheta_1}\bar{L}) & -i\bar{k} \sinh(\bar{\gamma}_{\Phi_1}\bar{L}) \\
\bar{\mathcal{T}}_{\varphi_1} \cosh(\bar{\gamma}_{\varphi_1}\bar{L}) & \bar{\mathcal{T}}_{\vartheta_1} \cosh(\bar{\gamma}_{\vartheta_1}\bar{L}) & 0 \\
\bar{\gamma}_{\varphi_1}\bar{\mathcal{H}}_1\bar{\mathcal{T}}_{\varphi_1} \sinh(\bar{\gamma}_{\varphi_1}\bar{L}) & \bar{\gamma}_{\vartheta_1}\bar{\mathcal{H}}_1\bar{\mathcal{T}}_{\vartheta_1} \sinh(\bar{\gamma}_{\vartheta_1}\bar{L}) & 0 \\
-2\bar{k}^2\bar{\mu}_2 + \bar{\alpha}_2\bar{T}_2\bar{K}_2\bar{\mathcal{T}}_{\varphi_2} + \bar{k}_{\varphi_2}^2\bar{\Gamma}_2 & -2\bar{k}^2\bar{\mu}_2 + \bar{\alpha}_2\bar{T}_2\bar{K}_2\bar{\mathcal{T}}_{\vartheta_2} + \bar{k}_{\vartheta_2}^2\bar{\Gamma}_2 & -\bar{\mu}_2(2\bar{k}^2 - \bar{k}_{\Phi_2}^2) \\
-i\bar{k} & -i\bar{k} & -2i\bar{\gamma}_{\Phi_2}\bar{k}\bar{\mu}_2 \\
\bar{\gamma}_{\varphi_2} & \bar{\gamma}_{\vartheta_2} & \bar{\gamma}_{\Phi_2} \\
-\bar{\mathcal{T}}_{\varphi_2} & -\bar{\mathcal{T}}_{\vartheta_2} & i\bar{k} \\
\bar{\gamma}_{\varphi_2}\bar{\mathcal{H}}_2\bar{\mathcal{T}}_{\varphi_2} & \bar{\gamma}_{\vartheta_2}\bar{\mathcal{H}}_2\bar{\mathcal{T}}_{\vartheta_2} & 0 \\
& & 0
\end{array} \right) = \bar{\mathbf{A}}_{Sym}. \tag{A.14}$$

When implementing this numerically however, we find that we must factorise (A.14) columnwise to achieve bounded trigonometric functions which is acceptable since it does not change the determinant. As a result, the DE that is passed to the solver is

$$\det \left( \begin{array}{ccc}
2i\bar{\gamma}_{\varphi_1}\bar{k}\bar{\mu}_1 \tanh(\bar{\gamma}_{\varphi_1}\bar{L}) & 2i\bar{\gamma}_{\vartheta_1}\bar{k}\bar{\mu}_1 \tanh(\bar{\gamma}_{\vartheta_1}\bar{L}) & \bar{\mu}_1(2\bar{k}^2 - \bar{k}_{\Phi_1}^2) \tanh(\bar{\gamma}_{\Phi_1}\bar{L}) \\
2\bar{k}^2\bar{\mu}_1 - \bar{\alpha}_1\bar{T}_1\bar{K}_1\bar{\mathcal{T}}_{\varphi_1} - \bar{k}_{\varphi_1}^2\bar{\Gamma}_1 & 2\bar{k}^2\bar{\mu}_1 - \bar{\alpha}_1\bar{T}_1\bar{K}_1\bar{\mathcal{T}}_{\vartheta_1} - \bar{k}_{\vartheta_1}^2\bar{\Gamma}_1 & -2i\bar{\gamma}_{\Phi_1}\bar{k}\bar{\mu}_1 \\
i\bar{k} & i\bar{k} & \bar{\gamma}_{\Phi_1} \\
\bar{\gamma}_{\varphi_1} \tanh(\bar{\gamma}_{\varphi_1}\bar{L}) & \bar{\gamma}_{\vartheta_1} \tanh(\bar{\gamma}_{\vartheta_1}\bar{L}) & -i\bar{k} \tanh(\bar{\gamma}_{\Phi_1}\bar{L}) \\
\bar{\mathcal{T}}_{\varphi_1} & \bar{\mathcal{T}}_{\vartheta_1} & 0 \\
\bar{\gamma}_{\varphi_1}\bar{\mathcal{H}}_1\bar{\mathcal{T}}_{\varphi_1} \tanh(\bar{\gamma}_{\varphi_1}\bar{L}) & \bar{\gamma}_{\vartheta_1}\bar{\mathcal{H}}_1\bar{\mathcal{T}}_{\vartheta_1} \tanh(\bar{\gamma}_{\vartheta_1}\bar{L}) & 0 \\
-2\bar{k}^2\bar{\mu}_2 + \bar{\alpha}_2\bar{T}_2\bar{K}_2\bar{\mathcal{T}}_{\varphi_2} + \bar{k}_{\varphi_2}^2\bar{\Gamma}_2 & -2\bar{k}^2\bar{\mu}_2 + \bar{\alpha}_2\bar{T}_2\bar{K}_2\bar{\mathcal{T}}_{\vartheta_2} + \bar{k}_{\vartheta_2}^2\bar{\Gamma}_2 & -\bar{\mu}_2(2\bar{k}^2 - \bar{k}_{\Phi_2}^2) \\
-i\bar{k} & -i\bar{k} & -2i\bar{\gamma}_{\Phi_2}\bar{k}\bar{\mu}_2 \\
\bar{\gamma}_{\varphi_2} & \bar{\gamma}_{\vartheta_2} & \bar{\gamma}_{\Phi_2} \\
-\bar{\mathcal{T}}_{\varphi_2} & -\bar{\mathcal{T}}_{\vartheta_2} & i\bar{k} \\
\bar{\gamma}_{\varphi_2}\bar{\mathcal{H}}_2\bar{\mathcal{T}}_{\varphi_2} & \bar{\gamma}_{\vartheta_2}\bar{\mathcal{H}}_2\bar{\mathcal{T}}_{\vartheta_2} & 0 \\
& & 0
\end{array} \right) = 0. \tag{A.15}$$

Similarly, for the antisymmetric modes we seek solutions of the form

$$\bar{\varphi}_1 = \bar{\mathbf{P}}1_A \sinh(\bar{\gamma}_{\varphi_1}\bar{y})e^{i\bar{k}\bar{x}}, \quad \bar{\varphi}_2(\bar{x}, \bar{y}) = \begin{cases} -\bar{\mathbf{P}}2_A e^{\bar{\gamma}_{\varphi_2}(\bar{y}+\bar{L})+i\bar{k}\bar{x}}, & \bar{y} \leq -\bar{L} \\ \bar{\mathbf{P}}2_A e^{-\bar{\gamma}_{\varphi_2}(\bar{y}-\bar{L})+i\bar{k}\bar{x}}, & \bar{y} \geq \bar{L} \end{cases}, \tag{A.16a}$$

$$\bar{\vartheta}_1 = \bar{\mathbf{T}}1_A \sinh(\bar{\gamma}_{\vartheta_1}\bar{y})e^{i\bar{k}\bar{x}}, \quad \bar{\vartheta}_2(\bar{x}, \bar{y}) = \begin{cases} -\bar{\mathbf{T}}2_A e^{\bar{\gamma}_{\vartheta_2}(\bar{y}+\bar{L})+i\bar{k}\bar{x}}, & \bar{y} \leq -\bar{L} \\ \bar{\mathbf{T}}2_A e^{-\bar{\gamma}_{\vartheta_2}(\bar{y}-\bar{L})+i\bar{k}\bar{x}}, & \bar{y} \geq \bar{L} \end{cases}, \tag{A.16b}$$

$$\bar{\Phi}_1 = \bar{\mathbf{S}}1_A \cosh(\bar{\gamma}_{\Phi_1}\bar{y})e^{i\bar{k}\bar{x}}, \quad \bar{\Phi}_2(\bar{x}, \bar{y}) = \begin{cases} \bar{\mathbf{S}}2_A e^{\bar{\gamma}_{\Phi_2}(\bar{y}+\bar{L})+i\bar{k}\bar{x}}, & \bar{y} \leq -\bar{L} \\ \bar{\mathbf{S}}2_A e^{-\bar{\gamma}_{\Phi_2}(\bar{y}-\bar{L})+i\bar{k}\bar{x}}, & \bar{y} \geq \bar{L} \end{cases}, \tag{A.16c}$$

for some complex valued amplitudes  $\bar{\mathbf{P}}1_A, \bar{\mathbf{P}}2_A, \bar{\mathbf{T}}1_A, \bar{\mathbf{T}}2_A, \bar{\mathbf{S}}1_A, \bar{\mathbf{S}}2_A$ . The resulting matrix  $\bar{\mathbf{A}}_{ASym}$  is then identical to (A.14) but with  $\cosh(\cdot)$  replaced by  $\sinh(\cdot)$  and viceversa and is therefore not included for brevity. The dispersion equation implemented in the numerics is given by

